

Article

The Lost South Gobi Microcontinent: Protolith Studies of Metamorphic Tectonites and Implications for the Evolution of Continental Crust in Southeastern Mongolia

Joshua P. Taylor ^{1,*}, Laura E. Webb ², Cari L. Johnson ³ and Matthew J. Heumann ⁴

¹ Department of Earth Sciences, 204 Heroy Geology Laboratory, Syracuse University, Syracuse, NY 13244, USA

² Department of Geology, University of Vermont, Burlington, VT 05405, USA;
E-Mail: lewebb@uvm.edu

³ Department of Geology and Geophysics, University of Utah, Salt Lake City, UT 84112, USA;
E-Mail: cari.johnson@utah.edu

⁴ ConocoPhillips Company, 600 North Dairy Ashford Rd., Houston, TX 77079, USA;
E-Mail: matthew.j.heumann@gmail.com

* Author to whom correspondence should be addressed; E-Mail: jtaylo03@gmail.com.

Received: 16 June 2013; in revised form: 22 July 2013 / Accepted: 3 August 2013 /

Published: 21 August 2013

Abstract: The Central Asian Orogenic Belt, or Altaids, is an amalgamation of volcanic arcs and microcontinent blocks that records a complex late Precambrian–Mesozoic accretionary history. Although microcontinents cored by Precambrian basement are proposed to play an integral role in the accretion process, a lack of isotopic data hampers volume estimates of newly produced arc-derived *versus* old-cratonic crust in southeastern Mongolia. This study investigates metamorphic tectonites in southern Mongolia that have been mapped as Precambrian in age, largely on the basis of their high metamorphic grade and high strain. Here we present results from microstructural analyses and U-Pb zircon geochronology on samples from Tavan Har (44.05° N, 109.55° E) and the Yagan-Onch Hayrhan metamorphic core complex (41.89° N, 104.24° E). Our results show no compelling evidence for Precambrian basement in southeastern Mongolia. Rather, the protoliths to all tectonites examined are Paleozoic–Mesozoic age rocks, formed during Devonian–Carboniferous arc magmatism and subsequent Permian–Triassic orogenesis during collision of the South Mongolia arc with the northern margin of China. These results yield important insights into the Paleozoic accretionary history of southern

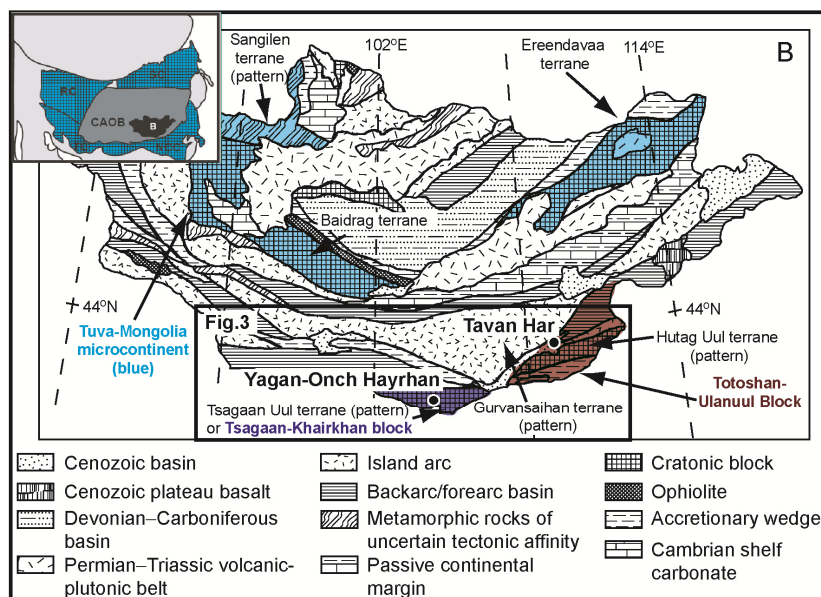
Mongolia, including the genesis of metamorphic and igneous basement during the Paleozoic, as well as implications for subsequent intracontinental reactivation.

Keywords: East Gobi Fault Zone; Central Asian Orogenic Belt; South Gobi Microcontinent; Yagan-Onch Hayrhan; Mongolia; Paleozoic; Mesozoic; tectonics; U-Pb geochronology

1. Introduction

Central Asia is an amalgamation of cratonic blocks, microcontinents and arc terranes that collided during the Paleozoic–Mesozoic to form the Central Asian Orogenic Belt (CAOB) [1,2] also known as the Altai [3,4] (Figure 1). The CAOB is a “natural laboratory” for the study of processes that lead to continental growth [4]. Many different models exist to describe the tectonic history of the CAOB, each of which incorporates Precambrian basement-cored microcontinents to varying degrees. This variation is largely due to the complex overprinting Mesozoic–Cenozoic structural history, through which the Paleozoic accretion history must be resolved, and the lack of detailed field studies and age constraints on many of the metamorphic and igneous rocks in the remote regions of Asia, such as Mongolia.

Figure 1. (A) Location of the Central Asian Orogenic Belt and surrounding Precambrian cratons. RC, Russian Craton; SC, Siberian Craton; TC, Tarim Craton; NCC, North China Craton. After Helo *et al.* [5]; (B) Terrane map of Mongolia modified from Badarch *et al.* [6]. Shaded regions denote general locations of mapped Precambrian microcontinents [7–10]; pattern regions represent terranes mapped as Precambrian by Badarch *et al.* [6].



The confirmation or invalidation of swaths of Precambrian basement throughout Mongolia has profound implications for the tectonic history of the CAOB, including the amount of juvenile crust present, previously estimated at 2.5 million km² [3], as well as the composition and strength of the crust during subsequent post-accretionary deformation. In the latter case, many models of Cenozoic deformation in response to the India-Asia collision propose that both cratonic blocks and

microcontinents act as rigid indenters and/or transfer stress, focusing deformation along weaker zones, commonly former sutures [11–16].

We use a number of terms to refer to microcontinents or fragments of microcontinents to preserve their names as published in western and eastern academic literature (such as block and terrane). In all cases we preserve the definition of a microcontinent as a rifted fragment of, in this case Precambrian, continental crust unless otherwise stated. In Mongolia, a number of microcontinents or fragments of microcontinents have been mapped (Figure 1). On the basis of U-Pb zircon geochronology, a Precambrian age has been confirmed for basement in some terranes such as in the Baidrag terrane [17]. In other examples, such as metamorphic units previously thought to be part of the Tuva-Mongolia microcontinent (Sangilen terrane of Badarch *et al.* [6]; Figure 1), a Precambrian age has been largely disproven through U-Pb zircon geochronology [8]. Our work focuses in particular on portions of the South Gobi Microcontinent.

The objectives of this study were to constrain the protoliths for key localities mapped as Precambrian basement in southeastern Mongolia [18,19] and to explore the implications of the results on the Paleozoic–Cenozoic tectonic history of the region. In southeastern Mongolia, high-grade and/or high-strain metamorphic tectonites have been inferred as Precambrian in age (Figure 2) [18,19] and interpreted to represent evidence for the presence of a microcontinent, which is featured in many terrane maps and Paleozoic reconstructions of the CAOB [2,3,6,9,20,21] (Figure 1). However, the actual age of these strongly deformed and/or metamorphosed rocks is questionable given the lack of supporting isotopic data and protolith constraints. Two Precambrian blocks, the Totoshan-Ulanuul block [10]; which contains the smaller Hutag Uul terrane of Badarch *et al.* [6] and the Tsagaan-Khairkhan block [22]; a.k.a., the Tsagaan Uul terrane of Badarch *et al.* [6] were previously proposed to underlie southeastern Mongolia on the basis of exposures of high-grade and/or high-strain tectonites (Figure 1). These two blocks together make up a large portion of the inferred South Gobi Microcontinent [8–10,21–23]. Recent studies have claimed to vindicate or have called into question a Precambrian age at a number of locations throughout southeastern Mongolia (in some cases within the same general area) emphasizing the need for further study [9,10,24–26].

Our study applied microstructural analysis and U-Pb zircon dating by laser ablation multicollector inductively coupled plasma mass spectrometry (LA-MC-ICPMS) to characterize samples from localities previously inferred to represent Precambrian basement [6,18,19]. We collected two samples at Tavan Har (Figure 3) in the Totoshan-Ulanuul block and five samples at Yagan-Onch Hayrhan (Figure 4) in the Tsagaan-Khairkhan block. Yagan-Onch Hayrhan is located in the Tsagaan Uul terrane of Badarch *et al.* [6] (Figure 1). The location of Tavan Har within the terrane classification of Badarch *et al.* [6] is less clear. It lies along the western side of the Zuunbayan basin, which places it within the Gurvansaihan island arc terrane on the basis of location. However, Tavan Har is mapped as a fault-bound basement block mainly composed of Precambrian metamorphic tectonites on regional geologic maps [6,19]. These mapped rocks have a tectonic affinity more in line with the metamorphic schists, gneisses, and migmatites that comprise the basement of the Hutag Uul terrane, located east of the Zuunbayan basin, than the early Paleozoic metasediments and late Paleozoic plutonic and volcanic rocks of the Gurvansaihan terrane [6]. We, therefore, consider Tavan Har the western edge of the Hutag Uul terrane.

Figure 2. Simplified geologic map of southeastern Mongolia and adjacent portions of northern China. Important Localities: HB, Han Bogd Pluton; TS, Tsagaan Subarga; MK, Mandakh Inlier; SK, Saykhandulaan Inlier. Geology in Mongolia is after Tomurtoogoo *et al.* [19]. Geology in China is after Zheng *et al.* [27].

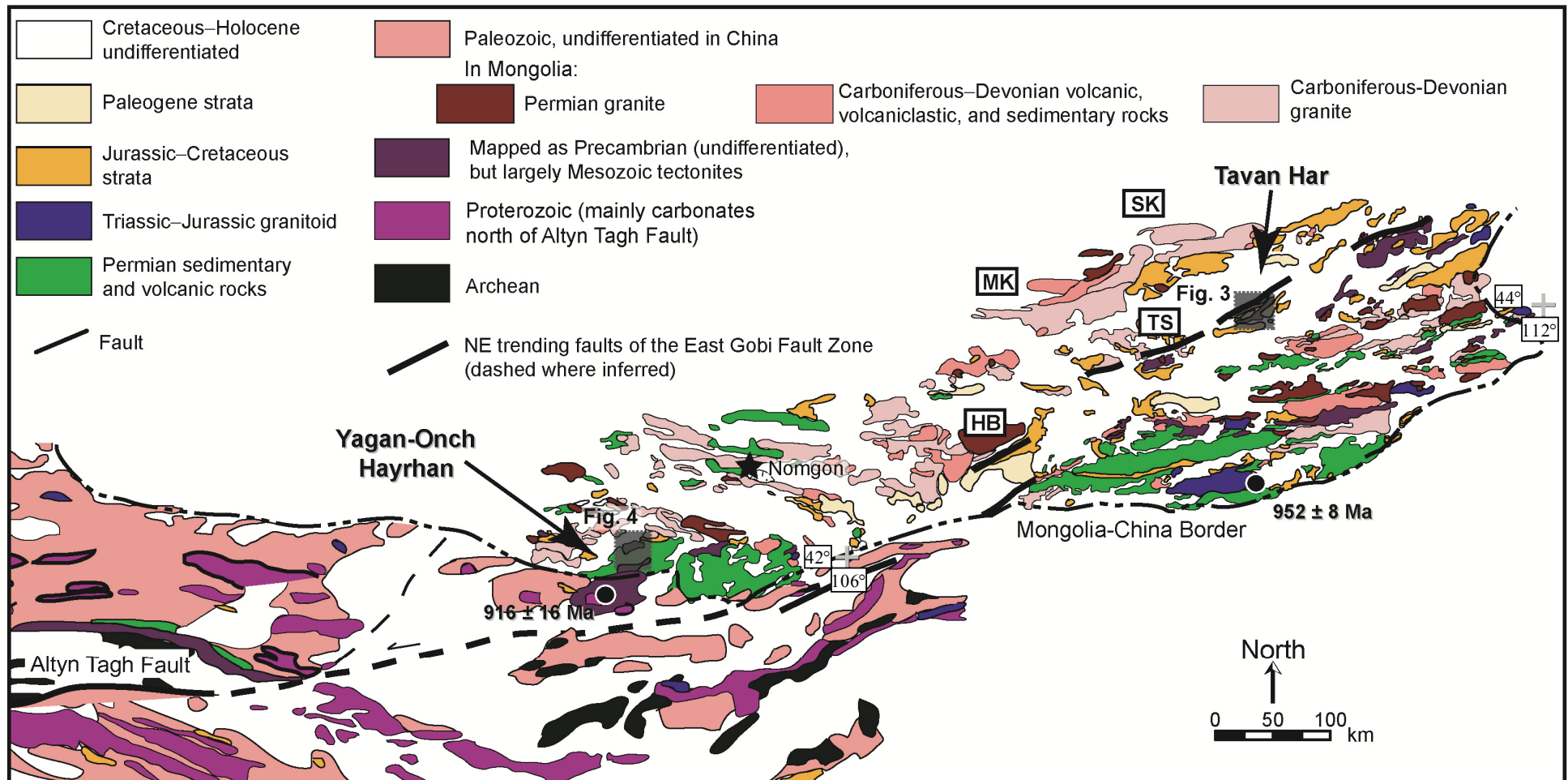


Figure 3. Geologic map of Tavan Har with sample locations. After Webb and Johnson [28].

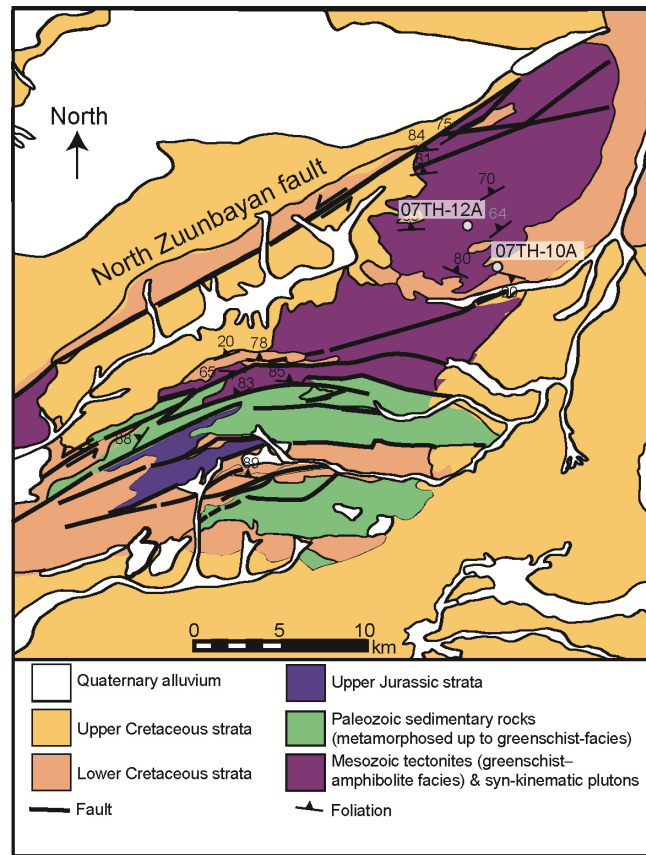
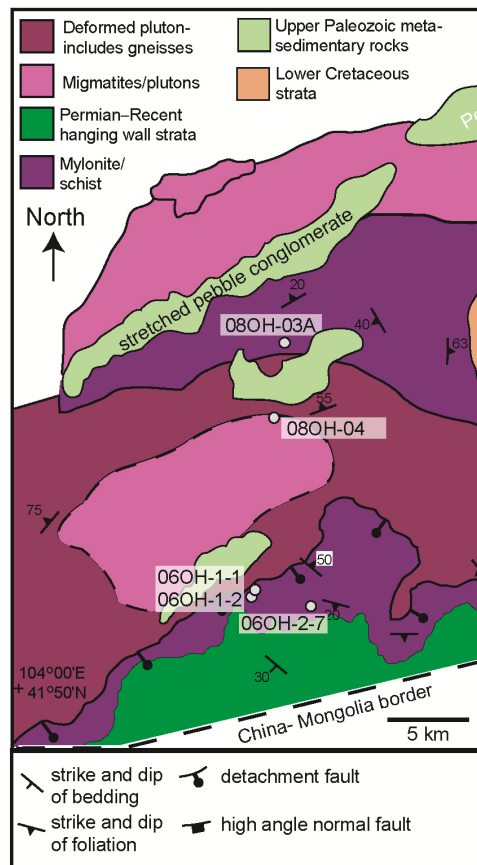


Figure 4. Geologic map of Yagan-Onch Hayrhan with sample locations. After Johnson *et al.* [29].



Yagan-Onch Hayrhan and Tavan Har are now separated by ~500 km across the East Gobi Fault Zone (EGFZ; Figure 2) [30,31], a NE-trending structural corridor with a polyphase Mesozoic–Cenozoic deformation history [26,28,32–34], but were located in closer proximity during the Paleozoic when ~270 km of total combined Late Triassic and Cenozoic sinistral displacement is restored [30]. Both regions have been relatively well mapped and studied with a focus on the Paleozoic–Cenozoic geologic history, making them ideal locations for our work [25–37].

2. Geologic Background

The Paleozoic rocks of southeastern Mongolia are mainly Late Silurian–late Carboniferous mafic to felsic volcanic and plutonic rocks largely originating within, or along, the South Mongolia arc. Smaller exposures of clastic and carbonate sedimentary rocks are also present [6,19,38,39]. Multiple large latest Silurian–earliest Devonian copper/gold/molybdenum deposits have been discovered (e.g., Oyu Tolgoi), which also formed within the South Mongolia arc [40–42]. All of the units described above are intruded by younger Late Permian–Early Triassic granitoids [6,19,23,38,39]. Devonian–Carboniferous age rocks in the southernmost portion of Mongolia, near the border with China, are overlain by Upper Permian–Lower Triassic clastic sedimentary rocks derived from the collision between the South Mongolia arc and the North China and Tarim cratons [19,37,43]. In the northern portion of the study region, metamorphic tectonites record deformation at upper amphibolite to greenschist-facies conditions, mainly during the Late Triassic [26]. Upper Triassic–Lower Jurassic strata were deposited in a foreland-style basin, followed by Late Jurassic–Early Cretaceous rift basin sedimentation during regional extension [29,31,32,44]. In the southern portion of the study region, extension was manifested in the formation of a metamorphic core complex [25,27,29,35,36]. Extension was also associated with the eruption of numerous basalt flows and intermediate–felsic tuff deposits [32,44,45]. Paleozoic–Early Cretaceous rocks are overlain by extensive Upper Cretaceous–Cenozoic variably lithified, mainly clastic, strata [19,29,32,44].

At Tavan Har and Yagan-Onch Hayrhan, previous structural geology, thermochronology, and basin analysis mainly focused on the Mesozoic–Present geologic history of the region; the results of these studies form an important framework upon which we can interpret the results of our work [25–37].

Tavan Har is a fault-bounded block within the northern portion of the EGFZ that has experienced a protracted deformation history, evidenced by the many faults that dissect the block (Figure 3). In the northern part of Tavan Har, amphibolite-facies gneisses, migmatites, and high-strain tectonites have been previously mapped as Precambrian [19]. This high-grade/high-strain deformation has largely been constrained as Triassic in age by $^{40}\text{Ar}/^{39}\text{Ar}$ dating, consisting of partial melting *ca.* 240 Ma (interpreted as minimum age) followed by sinistral strike-slip deformation at amphibolite to greenschist-facies conditions accompanied by syn-kinematic magmatism *ca.* 225–210 Ma [26].

Previous microstructural analysis of some tectonites (mapped as Precambrian) identified remnant primary volcanic textures indicating the protoliths were likely late Paleozoic volcanoclastic rocks, which are common throughout the region [26]. For our study, samples were collected from amphibolite-facies tectonites of the shear zone and from weakly deformed granitic gneiss inferred to be part of the syn-kinematic magmatic complex.

Yagan-Onch Hayrhan is located near the Mongolia-China border along the southwestern edge of the EGFZ. Its most notable feature is the exposure of a Late Jurassic–Early Cretaceous metamorphic core complex [25,27,29,35,36] (Figure 4) in which Precambrian rocks have been mapped in the footwall block [9,19].

The core complex contains syn-tectonic intrusions and amphibolite-facies to lower grade deformation fabrics that preserve a record of top-to-the-SE shear and progressively overprint an older amphibolite to greenschist facies top-to-the-SW fabric [25,29]. A zone of migmatites and variably deformed intrusions is exposed in the transition zone between these two fabrics. The age of the top-to-the-SW fabric is poorly constrained to the Triassic–Early Jurassic on the basis of cross-cutting relationships (it deformed Permian sedimentary rocks and is crosscut by Late Jurassic–Early Cretaceous metamorphic core complex fabrics). Field studies have identified a gradual transition from relatively undeformed sedimentary rocks to metasedimentary rocks with a top-to-the-SW shear sense, metamorphosed at greenschist-facies conditions [29]. A geochemical study of samples from Yagan-Onch Hayrhan by Wang *et al.* [9] determined a U-Pb age of 916 ± 16 (2σ) Ma for zircons from an augen gneiss deformed within Late Jurassic–Early Cretaceous metamorphic core complex, which they cite as the age of the protolith. Our study sampled rocks of the metamorphic core complex which record top-to-the-SE shear and rocks which preserve the older top-to-the-SW fabric.

3. Methods

3.1. Microstructural Analysis

Petrographic and microstructural analyses were conducted on each sample. For oriented samples, sections were cut parallel to the dominant lineation and perpendicular to the foliation. Primary textures, petrographic and textural relationships between mineral phases, and deformation microstructures were evaluated. Primary textures of interest included feldspar grains exhibiting igneous microstructures, such as a euhedral rectangular lath or square habits, magmatic twins or zoning, euhedral and/or lath-shaped poikilitic grains, and embayed quartz.

To understand the deformation history of each sample, we focused on quartz and feldspar microstructures. The temperature dependence (assuming strain rates in the range of 10^{-12} – 10^{-14} s⁻¹) of the dominant deformation mechanism(s) and resultant microstructure(s) has been extensively studied for quartz and to a lesser extent feldspar [46]. Multiple quartz and feldspar deformation microstructures were identified in our samples, some of which are relict textures only partially recrystallized during subsequent deformation.

3.2. Analytical Methods for U-Pb Zircon Geochronology

Zircons were acquired from rock samples using standard crushing and sieving techniques, followed by water, magnetic and heavy liquid separation techniques. Zircon separates were examined under a stereographic microscope at up to 288× magnification in ethyl alcohol to select inclusion-free zircons of various morphologies. Approximately 50–100 grains were picked from each sample and mounted in epoxy. All mounts were ground down to expose the interior of each grain and polished for imaging. To examine the internal morphology of each grain and identify inclusions not visible during selection

under 288× magnification, zircons were imaged in secondary electron and cathodoluminescence (CL) modes using a JEOL JXA8600 (JEOL, Tokyo, Japan) electron microprobe at Syracuse University.

Zircon U-Pb geochronology was conducted at the Arizona LaserChron Center using LA-MC-ICPMS [47,48]. The analyses involve ablation with a New Wave UP193HE Excimer laser (Electro Scientific Industries, Portland, OR, USA) (operating $\lambda = 193$ nm). During analyses, the ablated material was transported by a He carrier gas into the plasma source of a Nu HR ICPMS (Nu Instruments, Wrexham, UK) that was equipped with a flight tube of sufficient width that U, Th, and Pb isotopes were measured simultaneously. Measurements were made in static mode, using Faraday detectors with 3×10^{11} ohm resistors for ^{238}U , ^{232}Th , ^{208}Pb – ^{206}Pb , and a discrete dynode ion counter for ^{204}Pb and ^{202}Hg ; ion yields were ~ 0.8 mV/ppm. Each analysis consisted of one 12-second integration on peaks with the laser off (for background), 15 one-second integrations with the laser firing, and a 30-second delay to purge the previous sample and prepare for the next analysis. The small size and complex internal morphology of many grains required various beam sizes producing ablation pits of approximately 18, 14, and 10 μm in diameter. A large proportion of grains were analyzed using an ablation pit approximately 10 μm in diameter and 4 μm deep, excavating approximately 1 ng of material [49].

A common Pb correction was made using the measured ^{204}Pb and assuming an initial Pb composition from Stacey and Kramers [50] (with uncertainties of 1.5 for $^{206}\text{Pb}/^{204}\text{Pb}$ and 0.3 for $^{207}\text{Pb}/^{204}\text{Pb}$). ^{204}Hg interference with ^{204}Pb is accounted for by measurement of ^{202}Hg during laser ablation and subtraction of ^{204}Hg using the natural $^{202}\text{Hg}/^{204}\text{Hg}$ ratio of 4.35. This correction is not significant in most analyses due to the very low Hg background level.

Inter-element fractionation of Pb/U is generally $\sim 5\%$ – 10% but is up to 30% for samples analyzed from ~ 1 ng of material. Apparent fractionation of Pb isotopes is generally $< 0.2\%$. In-run analysis (generally every fifth measurement) of fragments of an internal standard with a known age of 563.5 ± 3.2 Ma (2σ error) is used to correct for fractionation [47]. The uncertainty resulting from the calibration correction is generally 1%–2% (2σ) for both $^{206}\text{Pb}/^{207}\text{Pb}$ and $^{206}\text{Pb}/^{238}\text{U}$ ages.

Concentrations of U and Th are calibrated relative to a well characterized Sri Lanka zircon which contains ~ 518 ppm of U and 68 ppm Th [48]. The analytical data are reported in Tables 1–7. Uncertainties shown in these tables are at the 1σ level, and include only analytical errors.

The Age Pick macro add-on program [51] for Microsoft Excel (Microsoft, Redmond, WA, USA) developed at the Arizona LaserChron Center was used in some cases to constrain a weighted mean age for a population of grains within a sample or grains from multiple samples. Age Pick calculates a weighted mean age, taking into account systematic errors. In Age Pick, outliers can be identified and excluded on the basis of uranium concentration, % concordance, and U/Th ratio. For other samples, weighted mean ages and probability distribution plots were calculated using Isoplot [52]. Analyses that were $> 30\%$ discordant (by comparison of $^{206}\text{Pb}/^{238}\text{U}$ and $^{206}\text{Pb}/^{207}\text{Pb}$ ages) or $> 5\%$ reversely discordant were discarded when calculating mean ages or plotting age probability distributions [47]. We used zircon morphology and zonation to guide interpretation of the U-Pb results when more than one age population is present.

Table 1. Laser ablation inductively coupled plasma mass spectrometry (LA-ICPMS) analytical data for 07TH-10A. All errors are given at the 1σ level. For ages younger than 1 Ga the ²⁰⁶Pb/²³⁸U age is used. For ages older than 1 Ga the ²⁰⁶Pb/²⁰⁷Pb age is used. Conc. = Concordance.

U-Pb geochronologic analyses 07TH10A				Isotope ratios							Apparent ages (Ma)								
Analysis	U (ppm)	²⁰⁶ Pb/ ²⁰⁴ Pb	U/Th	²⁰⁶ Pb/ ²⁰⁷ Pb	± (%)	²⁰⁷ Pb/ ²³⁵ U	± (%)	²⁰⁶ Pb/ ²³⁸ U	± (%)	error corr.	²⁰⁶ Pb/ ²³⁸ U (Ma)	± (Ma)	²⁰⁷ Pb/ ²³⁵ U (Ma)	± (Ma)	²⁰⁶ Pb/ ²⁰⁷ Pb (Ma)	± (Ma)	Conc. (%)	Pit Diameter (μm)	Population Age
07TH10A-2C-A	97	3283	1.6	18.7427	10.0	0.3524	12.9	0.0479	8.2	0.63	301.6	24.1	306.5	34.1	343.9	226.0	87.7	10	
07TH10A-40R-B	690	16382	0.9	19.1456	0.9	0.3406	7.6	0.0473	7.6	0.99	297.9	22.1	297.6	19.7	295.6	20.0	100.8	10	
07TH10A-15R-B	255	23527	1.2	18.7668	1.8	0.3487	3.3	0.0475	2.8	0.84	298.9	8.1	303.8	8.6	341.0	40.0	87.7	14	
07TH10A-16R-B	791	53157	1.6	18.8917	0.6	0.3665	2.2	0.0502	2.2	0.97	315.9	6.6	317.1	6.1	325.9	13.1	96.9	14	
07TH10A-18C-A	244	20813	2.4	18.6552	1.5	0.3601	4.8	0.0487	4.5	0.95	306.6	13.5	312.3	12.8	354.5	33.7	86.5	14	
07TH10A-27C-A	131	8685	2.3	18.7774	2.1	0.3576	2.5	0.0487	1.3	0.53	306.5	4.0	310.4	6.7	339.7	48.3	90.2	14	
07TH10A-36C-A	108	6155	2.0	18.8296	3.6	0.3525	4.4	0.0481	2.6	0.58	303.0	7.6	306.6	11.6	333.4	81.0	90.9	14	307 ± 6 Ma (2σ)
07TH10A-1C-A	130	4535	1.4	18.6180	5.7	0.4057	9.2	0.0548	7.3	0.79	343.9	24.3	345.8	27.0	358.9	128.3	95.8	10	
07TH10A-1R-B	201	13594	1.9	18.2333	4.7	0.4461	6.0	0.0590	3.7	0.61	369.5	13.2	374.5	18.8	405.9	106.3	91.0	10	
07TH10A-13R-B	266	8491	1.9	18.8436	3.3	0.3941	11.5	0.0539	11.0	0.96	338.2	36.4	337.4	33.1	331.7	75.7	101.9	10	
07TH10A-25C-A	285	10766	0.9	18.8083	2.1	0.3644	4.4	0.0497	3.9	0.88	312.7	11.8	315.5	12.0	336.0	47.8	93.1	10	
07TH10A-30C-A	185	7377	1.1	18.7801	4.5	0.3880	5.9	0.0528	3.8	0.65	332.0	12.4	332.9	16.8	339.4	102.2	97.8	10	
07TH10A-30R-B	278	12192	1.6	18.8128	2.0	0.3977	4.6	0.0543	4.1	0.90	340.7	13.7	340.0	13.3	335.4	46.1	101.6	10	
07TH10A-40C-A	156	5494	1.3	18.9022	3.0	0.3946	4.7	0.0541	3.5	0.76	339.7	11.7	337.8	13.4	324.7	69.1	104.6	10	
07TH10A-41C-A	189	6515	1.4	18.5462	3.3	0.3873	4.5	0.0521	3.1	0.69	327.4	10.0	332.4	12.9	367.7	73.9	89.0	10	
07TH10A-47C-A	253	6888	1.1	19.0453	1.8	0.3612	4.3	0.0499	3.9	0.91	313.9	11.9	313.1	11.6	307.5	41.5	102.1	10	
07TH10A-4C-A	264	18568	1.4	18.8124	1.0	0.3952	2.3	0.0539	2.1	0.90	338.5	6.9	338.2	6.7	335.5	22.8	100.9	14	
07TH10A-12C-A	262	28887	2.8	18.7075	1.1	0.4169	5.9	0.0566	5.8	0.98	354.7	19.9	353.8	17.6	348.1	25.2	101.9	14	
07TH10A-13C-A	204	12090	2.4	18.8453	2.5	0.3778	3.3	0.0516	2.1	0.64	324.6	6.7	325.4	9.2	331.5	57.1	97.9	14	
07TH10A-14C-A	204	14062	2.2	19.0091	1.7	0.3632	2.9	0.0501	2.4	0.82	314.9	7.4	314.6	7.9	311.9	37.8	101.0	14	
07TH10A-15C-A	162	11624	1.7	18.8436	2.6	0.3612	4.1	0.0494	3.1	0.77	310.6	9.5	313.1	11.0	331.7	59.1	93.6	14	
07TH10A-16C-A	143	8955	1.8	18.7501	2.4	0.3894	3.1	0.0530	1.9	0.62	332.6	6.2	333.9	8.8	343.0	54.8	97.0	14	
07TH10A-17R-A	84	416785	2.3	17.9806	2.4	0.3975	3.7	0.0518	2.8	0.76	325.8	9.0	339.8	10.7	437.0	53.7	74.5	14	
07TH10A-20C-A	118	15635	3.0	18.3582	6.2	0.3726	6.8	0.0496	2.7	0.40	312.1	8.3	321.6	18.6	390.6	139.0	79.9	14	
07TH10A-20R-B	143	24260	2.6	18.5587	3.0	0.4040	4.6	0.0544	3.5	0.76	341.3	11.7	344.5	13.5	366.1	67.8	93.2	14	

Table 1. Cont.

U-Pb geochronologic analyses 07TH10A				Isotope ratios							Apparent ages (Ma)								
Analysis	U (ppm)	²⁰⁶ Pb ²⁰⁴ Pb	U/Th	²⁰⁶ Pb ²⁰⁷ Pb	±	²⁰⁷ Pb ²³⁵ U	±	²⁰⁶ Pb ²³⁸ U	±	error corr.	²⁰⁶ Pb ²³⁸ U	±	²⁰⁷ Pb ²³⁵ U	±	²⁰⁶ Pb ²⁰⁷ Pb	±	Conc. (%)	Pit Diameter (µm)	Population Age
07TH10A-21C-B	387	32055	2.6	18.8082	0.9	0.3996	3.6	0.0545	3.5	0.97	342.2	11.6	341.4	10.4	336.0	20.7	101.8	14	
07TH10A-22C-A	231	24911	1.2	18.6840	1.3	0.3946	2.4	0.0535	2.0	0.84	335.8	6.6	337.7	6.9	351.0	29.1	95.7	14	
07TH10A-32C-A	233	12763	2.6	18.7738	1.7	0.3722	5.4	0.0507	5.1	0.95	318.7	15.9	321.3	14.9	340.1	38.3	93.7	14	
07TH10A-32R-B	261	14972	1.8	18.7843	1.1	0.3891	4.6	0.0530	4.5	0.97	332.9	14.6	333.7	13.2	338.8	24.3	98.3	14	
07TH10A-33C-A	148	12707	1.9	18.5337	2.0	0.4007	4.7	0.0539	4.3	0.91	338.2	14.1	342.1	13.7	369.2	44.6	91.6	14	
07TH10A-34C-A	264	45693	2.0	18.1059	4.4	0.3943	6.9	0.0518	5.3	0.77	325.4	16.9	337.5	19.8	421.5	97.7	77.2	14	
07TH10A-39C-A	196	27854	2.6	18.5501	2.3	0.4211	8.6	0.0567	8.3	0.96	355.2	28.5	356.8	25.8	367.2	52.7	96.7	14	
07TH10A-42C-A	153	14160	1.6	18.5197	1.7	0.4004	2.3	0.0538	1.6	0.67	337.7	5.1	341.9	6.7	370.9	38.6	91.0	14	
07TH10A-43C-A	399	88725	1.5	18.6151	0.7	0.4136	4.5	0.0558	4.4	0.99	350.3	15.0	351.5	13.2	359.3	16.3	97.5	14	
07TH10A-56C-A	234	41310	1.8	18.6712	0.9	0.4264	3.8	0.0577	3.7	0.97	361.8	13.1	360.6	11.6	352.5	19.3	102.6	14	
07TH10A-1R-C	497	8210	1.7	18.7978	1.5	0.4176	5.3	0.0569	5.1	0.96	357.0	17.6	354.3	15.8	337.2	33.4	105.8	10	
07TH10A-45C-A	286	7836	1.2	18.8220	2.5	0.4138	11.3	0.0565	11.0	0.97	354.2	38.1	351.6	33.7	334.3	57.4	106.0	10	
07TH10A-45R-B	814	19357	0.7	18.9175	1.0	0.4096	4.1	0.0562	4.0	0.97	352.5	13.7	348.6	12.2	322.9	22.7	109.2	10	
07TH10A-50C-A	134	3263	2.1	19.5736	6.4	0.3699	9.2	0.0525	6.7	0.72	329.9	21.4	319.6	25.3	244.8	146.9	134.7	10	331 ± 5 Ma (2σ)
07TH10A-5C-A	188	9474	2.8	19.0214	1.7	0.3924	3.0	0.0541	2.4	0.81	339.9	7.9	336.1	8.5	310.4	39.7	109.5	14	
07TH10A-6C-A	439	12993	2.0	19.1043	1.6	0.4660	6.4	0.0646	6.2	0.97	403.4	24.2	388.4	20.7	300.5	37.0	134.2	14	
07TH10A-10C-A	218	15288	1.3	19.0146	2.1	0.4115	7.9	0.0567	7.6	0.97	355.8	26.4	349.9	23.4	311.2	46.7	114.3	14	
07TH10A-21C-A	469	29761	1.9	19.0050	0.6	0.4626	6.9	0.0638	6.9	1.00	398.5	26.7	386.1	22.2	312.4	12.6	127.6	14	
07TH10A-35C-A	76	5463	1.9	19.2034	4.5	0.3809	5.1	0.0531	2.3	0.46	333.2	7.6	327.7	14.2	288.6	102.8	115.5	14	
07TH10A-51C-A	272	16145	1.8	18.7610	1.2	0.4217	3.4	0.0574	3.2	0.94	359.6	11.1	357.2	10.2	341.7	26.1	105.3	14	

Table 2. LA-ICPMS analytical data for 07TH-12A. All errors are given at the 1σ level. For ages younger than 1 Ga the ²⁰⁶Pb/²³⁸U age is used. For ages older than 1 Ga the ²⁰⁶Pb/²⁰⁷Pb age is used. Conc. = Concordance.

U-Pb geochronologic analyses 07TH12A				Isotope ratios							Apparent ages (Ma)								
Analysis	U (ppm)	²⁰⁶ Pb / ²⁰⁴ Pb	U/Th	²⁰⁶ Pb / ²⁰⁷ Pb	± (%)	²⁰⁷ Pb / ²³⁵ U	± (%)	²⁰⁶ Pb / ²³⁸ U	± (%)	error corr.	²⁰⁶ Pb / ²³⁸ U (Ma)	± (Ma)	²⁰⁷ Pb / ²³⁵ U (Ma)	± (Ma)	²⁰⁶ Pb / ²⁰⁷ Pb (Ma)	± (Ma)	Conc. (%)	Pit Diameter (μm)	Population Age
07TH12A-30R-B	862	14548	1.2	19.6391	1.5	0.2431	7.0	0.0346	6.9	0.98	219.4	14.8	220.9	13.9	237.2	34.0	92.5	10.0	
07TH12A-2R-B	266	5271	2.5	19.4957	5.7	0.2247	7.4	0.0318	4.7	0.64	201.6	9.4	205.8	13.8	254.0	131.0	79.4	10.0	
07TH12A-4C-A	71	2904	2.4	19.6888	5.9	0.2432	6.4	0.0347	2.6	0.40	220.1	5.6	221.1	12.8	231.3	135.8	95.2	14.0	
07TH12A-6C-A	86	3162	1.7	19.5426	4.8	0.2526	6.0	0.0358	3.5	0.59	226.8	7.9	228.7	12.2	248.5	110.7	91.3	14.0	
07TH12A-7R-B	98	4734	2.3	19.0180	5.3	0.2742	5.9	0.0378	2.6	0.44	239.3	6.1	246.1	12.9	310.8	120.4	77.0	14.0	
07TH12A-12C-A	79	3492	1.8	19.6414	6.2	0.2536	6.6	0.0361	2.3	0.35	228.7	5.2	229.5	13.5	236.9	142.0	96.5	14.0	
07TH12A-12R-B	119	6623	2.4	19.6235	5.3	0.2649	9.0	0.0377	7.3	0.81	238.6	17.0	238.6	19.1	239.0	121.8	99.8	14.0	
07TH12A-13C-A	87	3081	2.2	19.9777	5.7	0.2237	7.9	0.0324	5.5	0.69	205.7	11.1	205.0	14.7	197.6	132.8	104.1	14.0	
07TH12A-15C-A	98	5192	1.8	19.4746	5.0	0.2339	6.6	0.0330	4.3	0.66	209.5	9.0	213.4	12.7	256.5	114.7	81.7	14.0	
07TH12A-18C-A	150	9531	1.3	19.4390	2.7	0.2410	5.6	0.0340	5.0	0.88	215.4	10.6	219.2	11.1	260.8	61.1	82.6	14.0	
07TH12A-22C-A	131	6264	1.8	19.7964	2.7	0.2473	7.7	0.0355	7.3	0.94	224.9	16.0	224.3	15.6	218.7	63.2	102.8	14.0	
07TH12A-26C-A	128	5567	1.9	19.6399	4.3	0.2295	5.9	0.0327	4.0	0.68	207.4	8.2	209.8	11.2	237.0	100.0	87.5	14.0	
07TH12A-29C-A	126	6499	2.0	19.3420	2.9	0.2415	3.6	0.0339	2.0	0.57	214.8	4.3	219.7	7.0	272.2	67.0	78.9	14.0	
07TH12A-30C-A	141	9018	1.4	19.7237	2.8	0.2446	4.8	0.0350	4.0	0.82	221.7	8.6	222.2	9.6	227.2	63.8	97.6	14.0	
07TH12A-32C-A	199	9480	2.2	19.5070	2.0	0.2596	3.2	0.0367	2.5	0.77	232.5	5.6	234.3	6.7	252.7	47.0	92.0	14.0	
07TH12A-44C-A	129	50872	1.8	18.7181	3.7	0.2822	7.1	0.0383	6.0	0.85	242.4	14.3	252.4	15.8	346.9	84.7	69.9	14.0	
07TH12A-50C-A	138	4337	2.2	19.8491	3.7	0.2280	4.4	0.0328	2.4	0.54	208.2	4.9	208.5	8.3	212.5	85.9	97.9	14.0	220 ± 6 Ma (2σ)
07TH12A-10R-B	173	18910	2.5	19.1732	2.7	0.2859	3.7	0.0398	2.5	0.68	251.3	6.2	255.3	8.2	292.3	60.9	86.0	14.0	
07TH12A-11C-A	77	4366	2.0	19.2826	7.9	0.2866	11.0	0.0401	7.6	0.69	253.4	18.9	255.9	24.8	279.3	181.3	90.7	14.0	
07TH12A-9C-A	280	4198	1.3	19.9259	4.7	0.2359	10.8	0.0341	9.7	0.90	216.1	20.5	215.1	20.9	203.6	110.3	106.2	10.0	
07TH12A-14C-A	88	1328	2.2	22.1433	10.8	0.1987	12.7	0.0319	6.7	0.53	202.5	13.4	184.1	21.4	-47.0	262.5	-431.2	10.0	
07TH12A-14R-B	463	7551	2.7	20.1280	2.2	0.2107	7.2	0.0308	6.8	0.95	195.2	13.1	194.1	12.7	180.1	52.4	108.4	10.0	
07TH12A-21C-A	64	3439	2.4	17.1668	19.1	0.2583	20.0	0.0322	5.8	0.29	204.1	11.7	233.3	41.6	539.2	420.9	37.8	10.0	
07TH12A-25C-A	112	16835	1.9	17.2894	7.0	0.2637	8.0	0.0331	3.8	0.48	209.7	7.9	237.6	17.0	523.6	154.3	40.0	10.0	
07TH12A-25R-B	80	1899	2.4	18.7890	13.4	0.2489	17.2	0.0339	10.8	0.63	215.0	22.9	225.6	34.8	338.3	304.0	63.6	10.0	

Table 2. Cont.

U-Pb geochronologic analyses 07TH12A				Isotope ratios							Apparent ages (Ma)								
Analysis	U (ppm)	²⁰⁶ Pb/ ²⁰⁴ Pb	U/Th	²⁰⁶ Pb	±	²⁰⁷ Pb	±	²⁰⁶ Pb	±	error	²⁰⁶ Pb	±	²⁰⁷ Pb	±	²⁰⁶ Pb	±	Conc.	Pit Diameter	Population Age
				²⁰⁷ Pb	(%)	²³⁵ U	(%)	²³⁸ U	(%)	corr.	²³⁸ U	(Ma)	²³⁵ U	(Ma)	²⁰⁷ Pb	(Ma)	(%)	(µm)	
07TH12A-33C-A	84	1936	1.7	20.2623	11.4	0.2243	13.4	0.0330	7.0	0.52	209.1	14.3	205.5	24.9	164.6	267.8	127.0	10.0	
07TH12A-35C-A	152	1929	1.9	21.1065	8.3	0.2109	9.6	0.0323	4.7	0.50	204.8	9.6	194.3	16.9	68.4	197.5	299.6	10.0	
07TH12A-35R-B	175	2785	2.4	20.1678	8.3	0.2127	8.7	0.0311	2.9	0.33	197.5	5.5	195.8	15.6	175.5	193.1	112.5	10.0	
07TH12A-43C-A	189	2383	1.5	20.5935	8.0	0.2153	8.3	0.0322	2.2	0.27	204.0	4.4	198.0	14.9	126.6	187.9	161.1	10.0	
07TH12A-1C-A	77	11595	1.7	18.2948	7.0	0.2697	9.3	0.0358	6.0	0.65	226.7	13.5	242.5	20.0	398.3	158.0	56.9	14.0	
07TH12A-2C-A	73	3036	2.1	18.8898	7.1	0.2580	8.7	0.0353	4.9	0.57	223.9	10.9	233.0	18.1	326.2	162.1	68.6	14.0	
07TH12A-3C-A	122	3647	1.6	20.3121	4.1	0.2358	6.1	0.0347	4.5	0.74	220.2	9.7	215.0	11.8	158.9	96.6	138.6	14.0	
07TH12A-5C-A	248	24160	0.9	19.1772	3.1	0.2161	3.7	0.0301	1.9	0.52	190.9	3.6	198.6	6.6	291.8	71.8	65.4	14.0	
07TH12A-7C-A	60	7503	2.1	18.3715	7.6	0.2707	9.3	0.0361	5.4	0.58	228.4	12.1	243.2	20.2	389.0	171.1	58.7	14.0	
07TH12A-10C-A	85	2911	2.5	20.0357	7.7	0.2566	8.9	0.0373	4.5	0.50	236.0	10.4	231.9	18.4	190.9	179.1	123.6	14.0	
07TH12A-17C-A	83	5019	2.0	18.9501	6.2	0.2368	6.9	0.0326	3.0	0.44	206.5	6.1	215.8	13.5	318.9	141.7	64.8	14.0	
07TH12A-20C-A	71	2867	2.1	20.0096	6.9	0.2587	7.5	0.0375	3.0	0.40	237.6	7.1	233.6	15.7	193.9	159.6	122.5	14.0	

Table 3. LA-ICPMS analytical data for 08OH-03A. All errors are given at the 1σ level. For ages younger than 1 Ga the ²⁰⁶Pb/²³⁸U age is used. For ages older than 1 Ga the ²⁰⁶Pb/²⁰⁷Pb age is used. Conc. = Concordance.

U-Pb geochronologic analyses 08OH03A				Isotope ratios							Apparent ages (Ma)								
Analysis	U (ppm)	²⁰⁶ Pb/ ²⁰⁴ Pb	U/Th	²⁰⁶ Pb	±	²⁰⁷ Pb	±	²⁰⁶ Pb	±	error	²⁰⁶ Pb	±	²⁰⁷ Pb	±	²⁰⁶ Pb	±	Conc.	Pit Diameter	Population Age
				²⁰⁷ Pb	(%)	²³⁵ U	(%)	²³⁸ U	(%)	corr.	²³⁸ U	(Ma)	²³⁵ U	(Ma)	²⁰⁷ Pb	(Ma)	(%)	(µm)	
08OH03A-45C-A	285	4831	1.3	19.6881	4.8	0.2441	14.9	0.0349	14.1	0.95	220.9	30.6	221.8	29.7	231.4	112.0	95.5	10.0	
08OH03A-1C-B	841	83568	3.1	19.5463	1.1	0.2747	2.7	0.0389	2.5	0.91	246.2	6.0	246.4	6.0	248.1	25.6	99.3	14	
08OH03A-1R-A	1172	43232	1.8	19.5446	0.6	0.2810	4.7	0.0398	4.6	0.99	251.8	11.4	251.5	10.4	248.3	14.8	101.4	14	
08OH03A-23C-A	590	21947	1.7	19.4849	0.5	0.2984	3.8	0.0422	3.7	0.99	266.2	9.8	265.1	8.8	255.3	11.5	104.3	14	
08OH03A-25C-A	1322	158423	7.0	19.4655	0.7	0.2780	2.7	0.0392	2.6	0.97	248.2	6.3	249.1	5.9	257.6	15.3	96.3	14	
08OH03A-34C-A	1486	93908	4.2	19.4470	0.5	0.2722	2.9	0.0384	2.9	0.98	242.8	6.8	244.4	6.3	259.8	11.5	93.5	14	248 ± 6 Ma (2σ)

Table 3. Cont.

U-Pb geochronologic analyses 08OH03A				Isotope ratios							Apparent ages (Ma)								
Analysis	U (ppm)	²⁰⁶ Pb ²⁰⁴ Pb	U/Th	²⁰⁶ Pb	±	²⁰⁷ Pb	±	²⁰⁶ Pb	±	error	²⁰⁶ Pb	±	²⁰⁷ Pb	±	²⁰⁶ Pb	±	Conc.	Pit Diameter	Population Age
				²⁰⁷ Pb	(%)	²³⁵ U	(%)	²³⁸ U	(%)	corr.	²³⁸ U	(Ma)	²³⁵ U	(Ma)	²⁰⁷ Pb	(Ma)	(%)	(µm)	
08OH03A-6R-C	4159	1674	3.9	7.9610	15.6	0.5832	18.3	0.0337	9.4	0.52	213.5	19.8	466.5	68.4	2037.4	278.5	10.5	10.0	
08OH03A-13R-B	1717	4647	2.9	14.1499	4.1	0.3528	7.4	0.0362	6.1	0.83	229.3	13.8	306.9	19.5	947.9	83.2	24.2	10.0	
08OH03A-16C-A	3149	6127	0.3	15.5025	3.1	0.2380	13.6	0.0268	13.2	0.97	170.2	22.2	216.7	26.5	758.2	65.9	22.4	10.0	
08OH03A-16R-B	5334	3535	0.5	11.8104	4.9	0.2170	6.1	0.0186	3.6	0.59	118.7	4.3	199.4	11.1	1308.0	95.8	9.1	10.0	
08OH03A-21R-B	6729	1321	3.8	6.8464	14.8	0.5255	33.8	0.0261	30.4	0.90	166.1	49.9	428.8	118.9	2300.3	254.9	7.2	10.0	
08OH03A-26R-B	2701	13365	5.5	17.4207	3.6	0.2863	5.9	0.0362	4.7	0.80	229.1	10.5	255.7	13.3	507.0	78.4	45.2	10.0	
08OH03A-29C-A	2312	1801	0.6	8.5065	9.9	0.4515	14.6	0.0279	10.8	0.74	177.1	18.8	378.3	46.3	1919.4	178.4	9.2	10.0	
08OH03A-11R-B	6155	1545	1.0	7.4661	3.2	0.3222	6.6	0.0174	5.8	0.88	111.5	6.4	283.6	16.3	2150.2	55.4	5.2	14	
08OH03A-12R-A	1909	11891	4.0	16.6348	4.6	0.2954	6.6	0.0356	4.7	0.71	225.7	10.4	262.8	15.3	607.7	100.2	37.1	14	
08OH03A-13C-A	2716	2860	1.0	10.3461	17.8	0.4260	19.7	0.0320	8.5	0.43	202.8	16.9	360.3	60.0	1560.5	337.5	13.0	14	
08OH03A-19C-A	3339	1564	1.2	7.5220	14.7	0.5459	16.3	0.0298	7.2	0.44	189.2	13.4	442.3	58.6	2137.2	258.1	8.9	14	
08OH03A-19R-B	3675	2275	3.7	9.2310	11.4	0.5136	14.6	0.0344	9.1	0.63	217.9	19.5	420.9	50.2	1771.5	208.1	12.3	14	
08OH03A-26C-A	1354	8154	1.8	15.4394	14.1	0.3455	14.4	0.0387	2.6	0.18	244.7	6.2	301.4	37.5	766.8	298.9	31.9	14	
08OH03A-28C-A	2628	2338	1.0	9.6214	7.0	0.4427	9.7	0.0309	6.7	0.69	196.1	13.0	372.2	30.2	1695.5	128.8	11.6	14	
08OH03A-4C-B	120	4846	3.4	18.7982	8.8	0.3306	9.8	0.0451	4.4	0.45	284.2	12.3	290.0	24.8	337.2	198.9	84.3	10.0	
08OH03A-2C-A	115	6035	1.8	18.8918	2.3	0.3602	3.8	0.0493	3.0	0.78	310.5	9.0	312.3	10.2	325.9	53.3	95.3	14	
08OH03A-3R-B	306	12141	2.3	19.1568	1.2	0.3421	1.9	0.0475	1.5	0.77	299.4	4.3	298.8	4.9	294.2	27.8	101.7	14	
08OH03A-7C-A	81	6494	2.2	18.4826	4.7	0.3362	5.0	0.0451	1.8	0.36	284.2	4.9	294.3	12.8	375.4	105.2	75.7	14	
08OH03A-4R-A	189	2261	3.6	19.9484	7.0	0.3017	10.3	0.0437	7.6	0.74	275.4	20.5	267.7	24.4	201.0	162.6	137.1	10.0	
08OH03A-7R-B	283	4729	5.8	19.2121	7.4	0.3683	7.8	0.0513	2.3	0.29	322.7	7.2	318.4	21.3	287.6	170.5	112.2	10.0	
08OH03A-9C-A	175	3268	2.4	19.8148	5.3	0.3014	9.7	0.0433	8.1	0.84	273.4	21.8	267.5	22.8	216.6	123.1	126.2	10.0	
08OH03A-3C-A	291	32213	2.3	18.9828	1.0	0.3907	9.1	0.0538	9.0	0.99	337.7	29.7	334.9	25.9	315.0	22.7	107.2	14	
08OH03A-5C-A	51	2408	2.3	19.4584	7.4	0.3614	7.7	0.0510	2.0	0.27	320.7	6.4	313.3	20.6	258.4	169.7	124.1	14	
08OH03A-10C-A	133	10272	3.3	19.1482	4.2	0.3783	5.8	0.0525	3.9	0.68	330.1	12.6	325.8	16.0	295.3	96.3	111.8	14	
08OH03A-21R-C	723	11825	6.6	18.9036	2.5	0.3591	7.8	0.0492	7.4	0.95	309.8	22.4	311.5	21	324.5	57.8	95.5	10	
08OH03A-21C-A	561	6322	4.3	15.1000	13.1	0.5086	21.8	0.0557	17.4	0.80	249.5	59.1	417.5	74.6	813.5	274.6	43.0	10	

Table 4. LA-ICPMS analytical data for 08OH-04D. All errors are given at the 1σ level. For ages younger than 1 Ga the ²⁰⁶Pb/²³⁸U age is used. For ages older than 1 Ga the ²⁰⁶Pb/²⁰⁷Pb age is used. Conc. = Concordance.

U-Pb geochronologic analyses 08OH04D				Isotope ratios							Apparent ages (Ma)							Populations	
Analysis	U (ppm)	²⁰⁶ Pb/ ²⁰⁴ Pb	U/Th	²⁰⁶ Pb/ ²⁰⁷ Pb	± (%)	²⁰⁷ Pb/ ²³⁵ U	± (%)	²⁰⁶ Pb/ ²³⁸ U	± (%)	error corr.	²⁰⁶ Pb/ ²³⁸ U (Ma)	± (Ma)	²⁰⁷ Pb/ ²³⁵ U (Ma)	± (Ma)	²⁰⁶ Pb/ ²⁰⁷ Pb (Ma)	± (Ma)	Conc. (%)		Pit Diameter (μm)
08OH04D-3C-A	363	15781	2.0	19.4531	2.2	0.3026	8.9	0.0427	8.6	0.97	269.5	22.8	268.4	21.0	259.1	51.6	104.0	10	CORES
04OH04D-13C-A	582	21179	1.5	17.3138	4.4	0.5928	6.0	0.0744	4.1	0.69	462.9	18.3	472.7	22.6	520.5	95.6	88.9	10	
04OH04D-14C-A	131	26847	1.2	6.0561	0.6	10.2206	5.1	0.4489	5.1	0.99	2390.5	100.9	2454.9	47.1	2508.8	10.2	95.3	10	
04OH04D-18C-A	134	4518	2.5	20.9960	6.6	0.4237	7.1	0.0645	2.8	0.39	403.1	10.8	358.7	21.5	80.8	155.9	498.8	10	
08OH04D-26C-A	180	35086	6.1	12.1657	0.4	2.2844	8.0	0.2016	8.0	1.00	1183.7	86.3	1207.5	56.5	1250.3	8.2	94.7	10	
08OH04D-29C-A	281	9528	3.2	19.2768	2.3	0.3230	15.6	0.0452	15.5	0.99	284.8	43.1	284.2	38.8	280.0	52.1	101.7	10	
08OH04D-36R-B	202	19275	1.4	19.0986	4.6	0.3118	8.2	0.0432	6.8	0.83	272.6	18.2	275.6	19.8	301.2	104.6	90.5	10	
08OH04D-46C-A	126	14887	6.8	17.4322	3.4	0.5391	5.7	0.0682	4.5	0.80	425.0	18.7	437.8	20.1	505.6	73.8	84.1	10	
08OH04D-48C-A	258	12375	2.9	19.2739	2.9	0.2977	8.8	0.0416	8.3	0.94	262.8	21.3	264.6	20.4	280.3	66.6	93.8	10	
08OH04D-14R-B	236	364668	0.9	6.1297	0.5	9.5279	3.0	0.4236	2.9	0.99	2276.7	56.3	2390.2	27.3	2488.4	7.9	91.5	14	
08OH04D-1C-A	138	5499	3.2	19.8996	3.7	0.3460	9.4	0.0499	8.6	0.92	314.1	26.4	301.7	24.5	206.7	86.8	152.0	10	
04OH04D-15C-B	725	16355	1.4	16.6104	13.6	0.4000	15.5	0.0482	7.6	0.49	303.4	22.4	341.7	45.1	610.9	294.9	49.7	10	
04OH04D-19C-C	708	16751	3.2	18.5102	8.5	0.2662	9.1	0.0357	3.3	0.36	226.3	7.2	239.6	19.5	372.0	192.2	60.8	10	
04OH04D-22C-A	218	7304	2.7	19.9497	4.9	0.3508	8.8	0.0508	7.3	0.83	319.1	22.8	305.3	23.2	200.9	113.6	158.9	10	
08OH04D-23C-A	110	4643	0.5	21.5151	17.5	0.2463	19.5	0.0384	8.7	0.44	243.1	20.7	223.6	39.2	22.5	423.0	1078.4	10	
08OH04D-25C-A	171	4967	1.3	23.7226	10.1	0.2444	11.6	0.0420	5.7	0.49	265.5	14.8	222.0	23.0	-217.3	253.3	-122.2	10	
08OH04D-31C-A	350	15530	1.9	19.4714	3.2	0.3217	6.0	0.0454	5.1	0.85	286.4	14.2	283.2	14.7	256.9	72.5	111.5	10	
08OH04D-32C-A	145	2255	2.5	16.7595	10.1	0.3417	11.7	0.0415	5.9	0.51	262.4	15.1	298.5	30.1	591.5	218.5	44.4	10	
08OH04D-32R-B	208	3887	3.7	20.8932	10.8	0.2604	13.5	0.0395	8.1	0.60	249.5	19.9	235.0	28.4	92.5	256.9	269.8	10	
08OH04D-33C-A	234	10279	6.5	19.4506	3.8	0.4115	5.6	0.0581	4.2	0.75	363.8	14.9	350.0	16.7	259.4	86.3	140.3	10	
08OH04D-34C-A	262	9718	2.0	19.4594	3.0	0.3347	7.5	0.0472	6.9	0.92	297.5	20.1	293.1	19.2	258.3	69.9	115.2	10	
08OH04D-35C-A	434	19814	1.7	19.8131	2.4	0.2995	5.5	0.0430	5.0	0.90	271.6	13.2	266.0	13.0	216.8	56.7	125.3	10	
08OH04D-36C-A	230	16857	1.6	19.2635	5.6	0.3481	8.3	0.0486	6.1	0.74	306.1	18.3	303.3	21.7	281.5	127.5	108.7	10	
08OH04D-37C-A	146	6873	2.9	19.4751	4.6	0.3380	8.6	0.0477	7.3	0.84	300.6	21.4	295.6	22.1	256.5	106.5	117.2	10	
08OH04D-47C-A	125	3523	2.5	16.0830	4.9	0.3980	11.5	0.0464	10.4	0.90	292.5	29.8	340.2	33.3	680.2	105.4	43.0	10	

Table 4. Cont.

U-Pb geochronologic analyses 08OH04D				Isotope ratios							Apparent ages (Ma)								
Analysis	U (ppm)	²⁰⁶ Pb	U/Th	²⁰⁶ Pb	±	²⁰⁷ Pb	±	²⁰⁶ Pb	±	error	²⁰⁶ Pb	±	²⁰⁷ Pb	±	²⁰⁶ Pb	±	Conc.	Pit Diameter	Populations
		²⁰⁴ Pb		²⁰⁷ Pb		(%)		²³⁵ U			(%)		²³⁸ U		(%)				
08OH04D-50C-A	201	15939	2.0	18.4558	4.8	0.5465	9.6	0.0732	8.3	0.87	455.1	36.5	442.7	34.4	378.7	107.7	120.2	10	
08OH04D-6C-A	33	5379	2.2	16.7294	6.0	0.4406	6.6	0.0535	2.7	0.41	335.8	8.8	370.7	20.4	595.4	129.8	56.4	14	
04OH04D-11C-A	308	14943	1.3	19.2848	3.2	0.3205	6.8	0.0448	5.9	0.88	282.7	16.4	282.3	16.6	279.0	73.4	101.3	10	
08OH04D-24C-A	165	8433	0.5	19.4201	6.7	0.2843	9.5	0.0400	6.7	0.70	253.1	16.6	254.1	21.3	263.0	155.1	96.3	10	
08OH04D-45C-A	155	9680	1.5	18.8424	4.4	0.3368	6.2	0.0460	4.4	0.71	290.1	12.5	294.8	15.9	331.8	98.9	87.4	10	Needle-shaped
08OH04D-45R-B	630	18693	2.1	19.0879	1.4	0.3157	6.5	0.0437	6.4	0.98	275.8	17.2	278.6	15.9	302.4	31.0	91.2	10	Grains
08OH04D-17C-A	492	63260	3.4	19.2048	1.5	0.3014	4.0	0.0420	3.7	0.93	265.1	9.5	267.5	9.3	288.5	34.2	91.9	14	
08OH04D-48C-A	258	12375	2.9	19.2739	2.9	0.2977	8.8	0.0416	8.3	0.94	262.8	21.3	264.6	20.4	280.3	66.6	93.8	10	272 ± 12
04OH04D-19C-C	708	16751	3.2	18.5102	8.5	0.2662	9.1	0.0357	3.3	0.36	226.3	7.2	239.6	19.5	372.0	192.2	60.8	10	Ma (2σ)
04OH04D-22C-A	218	7304	2.7	19.9497	4.9	0.3508	8.8	0.0508	7.3	0.83	319.1	22.8	305.3	23.2	200.9	113.6	158.9	10	
08OH04D-33C-A	234	10279	6.5	19.4506	3.8	0.4115	5.6	0.0581	4.2	0.75	363.8	14.9	350.0	16.7	259.4	86.3	140.3	10	
08OH04D-34C-A	262	9718	2.0	19.4594	3.0	0.3347	7.5	0.0472	6.9	0.92	297.5	20.1	293.1	19.2	258.3	69.9	115.2	10	
08OH04D-10R-A	1945	28383	4.6	18.1474	2.6	0.3649	6.0	0.0480	5.4	0.90	302.4	15.9	315.9	16.2	416.4	58.0	72.6	10	
04OH04D-16C-A	173	11161	0.6	16.7562	1.9	0.3791	15.3	0.0461	15.2	0.99	290.3	43.0	326.4	42.6	592.0	40.2	49.0	10	
04OH04D-20C-A	421	14869	8.9	17.3914	1.5	0.3646	3.5	0.0460	3.2	0.90	289.9	9.0	315.7	9.5	510.8	32.8	56.8	10	
08OH04D-27C-A	209	8432	1.0	20.2453	4.3	0.3523	5.7	0.0517	3.7	0.65	325.1	11.6	306.4	15.0	166.6	101.1	195.2	10	
08OH04D-28C-A	137	30784	2.0	20.4665	3.6	0.2764	10.3	0.0410	9.6	0.94	259.2	24.4	247.8	22.5	141.1	84.4	183.7	10	
08OH04D-52C-A	950	7446	1.8	14.9439	22.0	0.3657	25.2	0.0396	12.4	0.49	250.6	30.5	316.5	68.7	835.2	462.7	30.0	10	
08OH04D-52R-B	1429	10582	1.3	15.3698	18.4	0.4035	29.4	0.0450	22.9	0.78	283.6	63.6	344.2	86.1	776.3	390.4	36.5	10	
08OH04D-1R-B	2829	1606	38.8	9.6970	9.2	0.2792	12.5	0.0196	8.5	0.68	125.4	10.5	250.0	27.7	1681.1	170.9	7.5	10	
08OH04D-4C-A	3376	2450	33.0	10.7637	6.9	0.2620	15.0	0.0204	13.3	0.89	130.5	17.1	236.2	31.6	1485.9	131.7	8.8	10	RIMS
04OH04D-15R-A	232	6259	11.6	23.7688	15.4	0.2807	17.7	0.0484	8.7	0.49	304.6	25.8	251.2	39.4	-222.2	389.7	-137.1	10	
04OH04D-19R-A	2474	2395	29.1	10.6793	4.2	0.2383	15.6	0.0185	15.0	0.96	117.9	17.6	217.0	30.5	1500.8	78.6	7.9	10	
04OH04D-19R-B	3031	7778	58.2	15.9313	29.2	0.1677	29.3	0.0194	3.1	0.11	123.7	3.8	157.5	42.8	700.4	633.5	17.7	10	
08OH04D-26R-B	1534	6668	47.5	13.6850	8.2	0.2284	19.6	0.0227	17.8	0.91	144.5	25.4	208.8	37.0	1015.9	167.3	14.2	10	

Table 4. Cont.

U-Pb geochronologic analyses 08OH04D				Isotope ratios							Apparent ages (Ma)							Populations	
Analysis	U (ppm)	²⁰⁶ Pb/ ²⁰⁴ Pb	U/Th	²⁰⁶ Pb/ ²⁰⁷ Pb	± (%)	²⁰⁷ Pb/ ²³⁵ U	± (%)	²⁰⁶ Pb/ ²³⁸ U	± (%)	error corr.	²⁰⁶ Pb/ ²³⁸ U (Ma)	± (Ma)	²⁰⁷ Pb/ ²³⁵ U (Ma)	± (Ma)	²⁰⁶ Pb/ ²⁰⁷ Pb (Ma)	± (Ma)	Conc. (%)		Pit Diameter (µm)
08OH04D-2C-A	242	12485	1.5	19.3532	4.0	0.3675	9.5	0.0516	8.6	0.91	324.3	27.3	317.8	26.0	270.9	91.4	119.7	10	Unclassified ages
08OH04D-2R-B	448	13958	1.9	19.2725	3.9	0.3783	9.1	0.0529	8.2	0.90	332.1	26.6	325.8	25.4	280.5	89.5	118.4	10	
08OH04D-7C-A	367	10506	2.7	19.7755	2.0	0.3218	3.4	0.0462	2.8	0.81	290.9	7.8	283.3	8.4	221.1	45.8	131.5	10	
08OH04D-9R-A	688	32327	7.6	18.2551	0.7	0.5027	3.0	0.0666	2.9	0.97	415.4	11.6	413.5	10.1	403.2	15.9	103.0	10	
08OH04D-9C-B	442	29528	22.1	18.5279	1.7	0.4411	4.6	0.0593	4.3	0.93	371.2	15.5	371.0	14.3	369.9	38.3	100.4	10	
04OH04D-12C-A	189	8491	1.8	17.9023	2.8	0.3632	5.6	0.0472	4.8	0.87	297.1	14.1	314.6	15.1	446.7	61.4	66.5	10	
04OH04D-12R-B	227	9776	2.8	19.8198	3.8	0.3275	5.8	0.0471	4.3	0.74	296.5	12.4	287.6	14.4	216.0	88.9	137.3	10	
08OH04D-30C-A	642	27262	1.0	18.7514	1.6	0.3519	2.0	0.0479	1.2	0.61	301.4	3.5	306.2	5.2	342.8	35.3	87.9	10	
08OH04D-38C-A	613	162246	1.0	18.3598	1.9	0.3847	3.1	0.0512	2.4	0.78	322.1	7.5	330.5	8.6	390.4	43.0	82.5	10	
08OH04D-40C-B	294	10576	1.4	19.4161	3.0	0.3725	24.6	0.0525	24.5	0.99	329.6	78.6	321.5	68.0	263.4	67.9	125.1	10	
08OH04D-40R-C	267	7849	1.8	18.8021	3.8	0.3097	7.7	0.0422	6.7	0.87	266.6	17.5	273.9	18.4	336.7	85.4	79.2	10	
08OH04D-43C-A	523	28901	1.7	19.1478	0.8	0.3967	4.3	0.0551	4.2	0.98	345.7	14.0	339.2	12.3	295.3	18.8	117.1	10	
08OH04D-43R-B	292	8367	2.2	19.3851	2.6	0.4353	6.7	0.0612	6.2	0.92	382.9	23.1	366.9	20.7	267.1	59.0	143.4	10	
08OH04D-51C-A	271	7005	2.3	19.0057	2.2	0.3407	6.3	0.0470	5.9	0.94	295.9	17.0	297.7	16.2	312.3	49.9	94.7	10	
08OH04D-10C-B	991	8369	3.0	15.5210	15.0	0.3852	17.4	0.0434	8.9	0.51	273.7	23.8	330.9	49.2	755.7	317.9	36.2	14	
08OH04D-1C-A	196	19691	1.4	17.9265	0.8	0.5740	1.9	0.0746	1.8	0.91	464.0	7.8	460.6	7.1	443.7	17.2	104.6	18	No CL image
08OH04D-2C-A	384	76305	5.2	5.8742	0.8	9.5768	6.3	0.4080	6.3	0.99	2205.8	117.2	2394.9	58.1	2560.0	12.6	86.2	18	No CL image
08OH04D-3C-A	112	7113	1.8	19.0911	2.8	0.3860	3.3	0.0535	1.7	0.52	335.7	5.6	331.5	9.3	302.1	64.0	111.1	18	No CL image
08OH04D-4C-A	339	22490	0.1	19.1067	1.3	0.3325	3.2	0.0461	2.9	0.91	290.4	8.2	291.4	8.0	300.2	29.4	96.7	18	No CL image
08OH04D-5C-A	157	9095	2.2	19.2323	1.9	0.3484	2.2	0.0486	1.1	0.51	305.9	3.3	303.5	5.8	285.2	43.6	107.2	18	No CL image
08OH04D-6C-A	3153	3304	4.0	11.5389	2.2	0.3124	2.8	0.0261	1.8	0.62	166.4	2.9	276.0	6.9	1353.0	43.2	12.3	18	No CL image
08OH04D-7C-A	463	6160	5.5	15.0577	12.8	0.2248	13.5	0.0246	4.2	0.31	156.4	6.5	205.9	25.1	819.4	267.9	19.1	18	No CL image
08OH04D-8C-A	883	67203	1.6	17.7948	0.4	0.5729	1.9	0.0739	1.8	0.97	459.9	8.0	459.9	6.9	460.1	9.3	99.9	18	No CL image
08OH04D-9C-A	878	91423	1.0	18.9206	0.5	0.3360	1.4	0.0461	1.3	0.94	290.6	3.6	294.1	3.5	322.5	10.7	90.1	18	No CL image
08OH04D-10C-A	474	52934	10.5	17.2854	3.5	0.5937	10.4	0.0744	9.8	0.94	462.8	43.8	473.2	39.3	524.2	76.0	88.3	18	No CL image
08OH04D-11C-A	334	33768	1.6	18.5644	1.1	0.4104	2.5	0.0553	2.2	0.90	346.7	7.5	349.1	7.3	365.5	24.2	94.9	18	No CL image
08OH04D-12C-A	296	11731	2.2	17.1476	3.2	0.5373	5.0	0.0668	3.9	0.77	416.9	15.7	436.6	17.9	541.7	69.8	77.0	18	No CL image
08OH04D-14C-A	105	7977	2.3	19.4891	3.0	0.3077	3.2	0.0435	1.0	0.30	274.4	2.6	272.4	7.6	254.8	69.9	107.7	18	No CL image
08OH04D-15C-A	252	19497	1.0	19.0408	1.2	0.3401	1.7	0.0470	1.2	0.72	295.9	3.5	297.2	4.4	308.0	26.7	96.0	18	No CL image

Table 5. LA-ICPMS analytical data for 06OH-1-2. All errors are given at the 1σ level. For ages younger than 1 Ga the ²⁰⁶Pb/²³⁸U age is used. For ages older than 1 Ga the ²⁰⁶Pb/²⁰⁷Pb age is used. Conc. = Concordance.

U-Pb geochronologic analyses 06OH1-2				Isotope ratios							Apparent ages (Ma)							Population Age
Analysis	U (ppm)	²⁰⁶ Pb/ ²⁰⁴ Pb	U/Th	²⁰⁶ Pb/ ²⁰⁷ Pb	± (%)	²⁰⁷ Pb/ ²³⁵ U	± (%)	²⁰⁶ Pb/ ²³⁸ U	± (%)	error corr.	²⁰⁶ Pb/ ²³⁸ U (Ma)	± (Ma)	²⁰⁷ Pb/ ²³⁵ U (Ma)	± (Ma)	²⁰⁶ Pb/ ²⁰⁷ Pb (Ma)	± (Ma)	Conc. (%)	
06OH12-3C-A	281	16026	2.6	17.5988	1.7	0.4480	6.7	0.0572	6.5	0.97	358.5	22.7	375.9	21.2	484.7	38.6	74.0	10.0
06OH12-10C-A	152	5927	4.3	17.4435	4.6	0.4508	8.8	0.0570	7.5	0.85	357.6	26.0	377.9	27.7	504.2	101.1	70.9	10.0
06OH12-11C-A	289	17575	3.1	17.4615	2.5	0.4705	10.0	0.0596	9.6	0.97	373.1	35.0	391.5	32.4	501.9	55.0	74.3	10.0
06OH12-13C-A	357	28357	2.6	18.4788	3.0	0.4226	9.9	0.0566	9.4	0.95	355.1	32.6	357.9	29.9	375.9	66.7	94.5	10.0
06OH12-17C-A	297	17862	2.5	18.1970	2.6	0.4338	6.0	0.0572	5.3	0.90	358.9	18.7	365.8	18.3	410.3	59.1	87.5	10.0
06OH12-18C-A	309	25101	2.2	17.3205	1.5	0.4788	2.6	0.0601	2.1	0.82	376.5	7.7	397.2	8.5	519.7	32.4	72.4	10.0
06OH12-23C-A	301	15015	2.1	18.1116	3.1	0.4418	15.5	0.0580	15.2	0.98	363.6	53.9	371.5	48.4	420.8	68.7	86.4	10.0
06OH12-26C-A	545	33388	2.9	18.1857	1.4	0.4122	9.7	0.0544	9.6	0.99	341.3	31.9	350.5	28.8	411.7	30.7	82.9	10.0
06OH12-27C-A	346	26676	2.1	17.9476	0.7	0.4500	5.9	0.0586	5.9	0.99	366.9	20.9	377.3	18.6	441.1	14.7	83.2	10.0
06OH12-30C-A	293	12778	2.7	18.2670	3.3	0.4479	9.2	0.0593	8.6	0.93	371.6	31.1	375.8	29.0	401.7	74.0	92.5	10.0
06OH12-37C-A	161	6680	2.4	18.2991	2.4	0.4557	7.3	0.0605	6.9	0.94	378.5	25.3	381.3	23.2	397.8	53.7	95.2	10.0
06OH12-55C-A	354	11842	2.4	17.4789	1.9	0.4703	5.3	0.0596	4.9	0.93	373.3	17.8	391.4	17.1	499.7	41.6	74.7	10.0
06OH12-67C-A	339	17323	2.0	18.3952	1.6	0.4368	7.5	0.0583	7.3	0.98	365.2	25.9	368.0	23.1	386.1	36.8	94.6	10.0
06OH12-1C-A	201	27527	2.8	18.2801	1.2	0.4345	2.2	0.0576	1.8	0.84	361.1	6.5	366.4	6.7	400.1	26.5	90.2	14.0
06OH12-2C-A	287	33783	2.6	18.4466	2.0	0.4495	4.4	0.0601	3.9	0.89	376.5	14.3	376.9	13.9	379.8	45.6	99.1	14.0
06OH12-12C-A	226	20389	2.3	18.5202	1.4	0.4483	4.9	0.0602	4.7	0.96	376.9	17.1	376.1	15.3	370.8	31.3	101.7	14.0
06OH12-14C-A	202	122235	2.4	18.5405	2.2	0.4481	4.5	0.0603	3.9	0.87	377.2	14.4	375.9	14.2	368.4	50.2	102.4	14.0
06OH12-15C-A	344	45526	2.0	18.4726	1.0	0.4345	1.7	0.0582	1.5	0.83	364.7	5.2	366.3	5.4	376.6	21.6	96.8	14.0
06OH12-2R-B	258	10511	2.6	18.7933	2.7	0.4205	6.8	0.0573	6.2	0.92	359.3	21.8	356.4	20.4	337.8	60.3	106.4	10.0
06OH12-4C-A	301	45948	2.0	18.7615	1.9	0.4437	4.0	0.0604	3.5	0.87	377.9	12.8	372.8	12.4	341.6	43.7	110.6	14.0

367 ± 9 Ma (2σ)

Table 6. LA-ICPMS analytical data for 06OH-1-1. All errors are given at the 1σ level. For ages younger than 1 Ga the ²⁰⁶Pb/²³⁸U age is used. For ages older than 1 Ga the ²⁰⁶Pb/²⁰⁷Pb age is used. Conc. = Concordance.

U-Pb geochronologic analyses 06OH1-1				Isotope ratios							Apparent ages (Ma)								
Analysis	U (ppm)	²⁰⁶ Pb/ ²⁰⁴ Pb	U/Th	²⁰⁶ Pb/ ²⁰⁷ Pb	± (%)	²⁰⁷ Pb/ ²³⁵ U	± (%)	²⁰⁶ Pb/ ²³⁸ U	± (%)	error corr.	²⁰⁶ Pb/ ²³⁸ U (Ma)	± (Ma)	²⁰⁷ Pb/ ²³⁵ U (Ma)	± (Ma)	²⁰⁶ Pb/ ²⁰⁷ Pb (Ma)	± (Ma)	Conc. (%)	Pit Diameter (μm)	Population Age
06OH11-34C-A	208	10133	1.8	18.8983	3.4	0.3936	7.1	0.0540	6.2	0.88	338.8	20.4	337.0	20.2	325.2	76.5	104.2	10	
06OH11-34C-B	232	17180	1.8	18.2213	2.5	0.4459	6.6	0.0589	6.1	0.92	369.1	21.9	374.4	20.7	407.4	56.3	90.6	10	
06OH11-45C-A	273	12787	1.7	18.2597	2.6	0.4438	6.3	0.0588	5.7	0.91	368.1	20.6	372.9	19.7	402.6	58.8	91.4	10	
06OH11-2C-A	318	73181	2.3	18.5117	1.1	0.4464	4.1	0.0599	3.9	0.96	375.3	14.3	374.8	12.8	371.9	25.7	100.9	14	
06OH11-3C-A	243	63889	2.0	18.2797	0.9	0.4389	2.0	0.0582	1.8	0.91	364.6	6.4	369.4	6.2	400.2	19.1	91.1	14	
06OH11-8C-A	218	56817	2.3	18.3886	1.4	0.4504	2.8	0.0601	2.4	0.87	376.0	8.8	377.5	8.7	386.9	31.0	97.2	14	
06OH11-9C-A	223	26251	1.8	18.5631	1.0	0.4505	3.7	0.0606	3.6	0.96	379.6	13.2	377.6	11.7	365.6	23.0	103.8	14	
06OH11-12C-A	321	66194	1.9	18.2201	0.9	0.4424	2.0	0.0585	1.7	0.89	366.3	6.2	372.0	6.1	407.5	19.8	89.9	14	
06OH11-13C-A	167	18951	2.5	18.5778	2.4	0.4404	3.3	0.0593	2.2	0.69	371.6	8.1	370.6	10.1	363.8	53.2	102.1	14	
06OH11-13R-B	310	71278	2.1	18.2881	0.8	0.4519	3.0	0.0599	2.9	0.96	375.2	10.5	378.6	9.4	399.1	17.9	94.0	14	
06OH11-17C-A	347	357144	1.9	18.3388	1.2	0.4385	4.1	0.0583	3.9	0.95	365.4	13.9	369.2	12.7	392.9	27.8	93.0	14	
06OH11-18C-A	2183	108416	2.5	18.1517	0.5	0.4751	2.1	0.0626	2.1	0.98	391.1	7.8	394.7	6.9	415.9	10.4	94.0	14	
06OH11-19C-A	256	256939	2.0	18.2377	1.5	0.4526	3.2	0.0599	2.8	0.88	374.8	10.3	379.1	10.2	405.3	34.5	92.5	14	
06OH11-20C-A	181	83057	2.3	18.0970	1.2	0.4618	6.4	0.0606	6.3	0.98	379.4	23.2	385.5	20.6	422.6	27.0	89.8	14	
06OH11-24C-A	345	93346	2.0	18.3518	0.8	0.4720	6.4	0.0628	6.3	0.99	392.8	24.0	392.6	20.7	391.4	17.2	100.4	14	
06OH11-62C-A	207	34838	2.2	18.3751	1.1	0.4583	2.8	0.0611	2.5	0.91	382.2	9.3	383.1	8.8	388.5	24.9	98.4	14	373 ± 8 Ma (2σ)
06OH11-7R-B	147	6621	7.5	17.0224	3.9	0.4583	6.6	0.0566	5.3	0.81	354.8	18.3	383.1	21.0	557.7	85.3	63.6	10	
06OH11-14R-A	212	10521	3.0	19.0848	3.5	0.4150	10.0	0.0574	9.4	0.94	360.0	32.8	352.4	29.7	302.8	78.7	118.9	10	
06OH11-1C-A	429	5215	1.2	12.9663	22.9	0.6644	28.0	0.0625	16.0	0.57	390.7	60.8	517.3	113.9	1124.4	463.0	34.7	14	
06OH11-10C-A	261	25994	2.2	18.5016	1.1	0.4726	7.1	0.0634	7.1	0.99	396.4	27.1	393.0	23.3	373.1	24.7	106.2	14	
06OH11-7C-A	539	30288	21.8	17.5502	0.6	0.5389	6.6	0.0686	6.5	1.00	427.7	27.0	437.7	23.3	490.8	13.3	87.1	10	
06OH11-7C-C	127	19294	87.2	17.5937	2.7	0.6419	6.7	0.0819	6.1	0.91	507.5	29.6	503.5	26.4	485.3	60.6	104.6	14	

Table 7. LA-ICPMS analytical data for 06OH-2-7. All errors are given at the 1σ level. For ages younger than 1 Ga the ²⁰⁶Pb/²³⁸U age is used. For ages older than 1 Ga the ²⁰⁶Pb/²⁰⁷Pb age is used. Conc. = Concordance.

U-Pb geochronologic analyses 06OH2-7			Isotope ratios								Apparent ages (Ma)								
Analysis	U (ppm)	²⁰⁶ Pb/ ²⁰⁴ Pb	U/Th	²⁰⁶ Pb/ ²⁰⁷ Pb	± (%)	²⁰⁷ Pb/ ²³⁵ U	± (%)	²⁰⁶ Pb/ ²³⁸ U	± (%)	error corr.	²⁰⁶ Pb/ ²³⁸ U (Ma)	± (Ma)	²⁰⁷ Pb/ ²³⁵ U (Ma)	± (Ma)	²⁰⁶ Pb/ ²⁰⁷ Pb (Ma)	± (Ma)	Conc. (%)	Pit Diameter (μm)	Population Age
06OH27-1C-A	241	17314	2.2	18.2638	1.2	0.4689	4.3	0.0621	4.1	0.96	388.4	15.6	390.4	14.0	402.1	26.9	96.6	10	
06OH27-2C-A	233	27488	2.1	18.5555	1.3	0.4282	5.0	0.0576	4.8	0.97	361.2	16.8	361.9	15.1	366.5	28.3	98.5	10	
06OH27-7R-B	273	25043	2.6	18.5036	2.2	0.4107	6.9	0.0551	6.5	0.95	345.8	21.9	349.4	20.3	372.8	49.5	92.8	10	
06OH27-11C-A	190	16866	1.4	18.0268	2.3	0.4477	4.8	0.0585	4.3	0.88	366.7	15.2	375.7	15.2	431.3	51.5	85.0	10	
06OH27-11R-B	142	19778	2.1	18.6371	4.4	0.4354	7.2	0.0588	5.7	0.79	368.6	20.4	367.0	22.2	356.6	99.6	103.4	10	
06OH27-5C-A	175	22571	2.6	18.6416	2.8	0.4345	5.8	0.0587	5.1	0.88	368.0	18.2	366.3	17.8	356.1	62.3	103.3	14	368 ± 14 Ma (2σ)
06OH27-1C-B	198	11490	2.3	18.9481	3.0	0.4474	7.0	0.0615	6.3	0.90	384.6	23.4	375.4	21.9	319.1	69.2	120.5	10	
06OH27-2R-B	322	17191	3.1	18.9658	2.0	0.4184	9.8	0.0576	9.6	0.98	360.8	33.8	354.9	29.5	317.0	46.1	113.8	10	
06OH27-7C-A	123	3530	3.7	16.8762	5.1	0.5088	6.3	0.0623	3.7	0.58	389.4	13.8	417.6	21.6	576.5	111.4	67.6	10	
06OH27-31C-A	217	17674	2.7	18.6811	2.1	0.4573	4.3	0.0620	3.7	0.87	387.5	14.0	382.4	13.6	351.3	46.8	110.3	14	
06OH27-2R-B	119	10101	2.8	18.6636	1.2	0.4432	2.6	0.0600	2.3	0.88	375.6	8.2	372.5	8.0	353.5	27.1	106.3	18	
06OH27-3C-A	276	20619	2.1	18.1336	2.3	0.4615	4.4	0.0607	3.8	0.86	379.9	13.9	385.3	14.1	418.1	50.6	90.9	10	
06OH27-4C-A	461	22128	2.1	17.6588	2.0	0.5066	3.0	0.0649	2.2	0.73	405.2	8.5	416.2	10.1	477.1	45.0	84.9	10	
06OH27-6C-A	199	18183	2.1	18.3500	2.7	0.4535	5.9	0.0603	5.3	0.89	377.7	19.4	379.7	18.7	391.6	59.7	96.5	10	
06OH27-8C-A	117	23266	2.4	17.8405	2.3	0.4968	4.6	0.0643	4.0	0.87	401.6	15.7	409.5	15.6	454.4	51.1	88.4	14	
06OH27-10C-B	1703	172865	1.5	18.3618	0.4	0.4571	3.3	0.0609	3.3	0.99	381.0	12.1	382.3	10.5	390.1	9.1	97.6	14	
06OH27-23C-A	1602	160095	1.4	18.3480	0.4	0.4769	2.6	0.0635	2.5	0.99	396.6	9.8	395.9	8.4	391.8	8.6	101.2	14	
06OH27-24C-A	169	10231	2.4	17.9866	2.7	0.4793	4.2	0.0625	3.2	0.76	391.0	12.2	397.6	13.9	436.3	60.9	89.6	14	
06OH27-42C-A	320	23579	2.2	18.2069	0.8	0.4526	5.2	0.0598	5.1	0.99	374.2	18.5	379.1	16.3	409.1	18.5	91.5	14	393 ± 9 Ma (2σ)

Table 7. Cont.

U-Pb geochronologic analyses 06OH2-7			Isotope ratios								Apparent ages (Ma)								
Analysis	U (ppm)	²⁰⁶ Pb ²⁰⁴ Pb	U/Th	²⁰⁶ Pb ²⁰⁷ Pb	± (%)	²⁰⁷ Pb ²³⁵ U	± (%)	²⁰⁶ Pb ²³⁸ U	± (%)	error corr.	²⁰⁶ Pb ²³⁸ U	± (Ma)	²⁰⁷ Pb ²³⁵ U	± (Ma)	²⁰⁶ Pb ²⁰⁷ Pb	± (Ma)	Conc. (%)	Pit Diameter (µm)	Population Age
06OH27-6C-B	250	22096	1.9	18.8614	3.1	0.4521	8.5	0.0618	8.0	0.93	386.8	29.9	378.7	27.0	329.6	70.2	117.4	10	
06OH27-8R-B	129	23680	3.4	18.4147	2.7	0.5187	4.0	0.0693	3.0	0.75	431.8	12.6	424.3	14.0	383.7	60.0	112.5	14	
06OH27-10C-A	1501	187198	1.4	18.4976	0.4	0.4732	2.7	0.0635	2.7	0.99	396.7	10.3	393.4	8.8	373.6	8.0	106.2	14	
06OH27-14C-A	1219	201214	1.6	18.4124	0.3	0.4981	2.5	0.0665	2.5	0.99	415.1	9.9	410.4	8.4	384.0	6.3	108.1	14	
06OH27-15C-A	221	8480	2.5	18.8255	1.5	0.4734	6.3	0.0646	6.1	0.97	403.7	24.0	393.5	20.6	333.9	34.0	120.9	14	
06OH27-27C-A	228	23109	2.2	18.7839	3.1	0.4761	5.6	0.0649	4.6	0.83	405.1	18.2	395.4	18.4	338.9	71.2	119.5	14	
06OH27-32C-A	225	87293	2.1	18.4138	1.7	0.5012	3.5	0.0669	3.1	0.88	417.7	12.4	412.5	11.8	383.8	37.1	108.8	14	
06OH27-34C-A	1449	126676	1.6	18.3386	0.4	0.5135	8.7	0.0683	8.7	1.00	425.9	35.7	420.8	29.9	393.0	8.8	108.4	14	
06OH27-13C-A	1893	115437	110.5	19.5422	0.3	0.2681	6.4	0.0380	6.4	1.00	240.4	15.0	241.2	13.7	248.6	6.4	96.7	14	252 ± 22 Ma (2σ)
06OH27-13C-B	1760	144303	72.1	19.3618	0.4	0.3003	6.5	0.0422	6.4	1.00	266.3	16.8	266.6	15.1	269.8	9.7	98.7	14	Metamorphic
06OH27-1-A	877	63928	2.0	18.4257	0.3	0.4401	1.1	0.0588	1.1	0.97	368.4	3.8	370.3	3.4	382.3	5.9	96.4	18	No CL image
06OH27-2-A	260	30283	2.6	18.3666	1.0	0.4308	2.0	0.0574	1.8	0.88	359.7	6.2	363.7	6.2	389.5	21.5	92.3	18	No CL image
06OH27-3-A	405	22008	2.0	18.5604	1.0	0.4223	4.2	0.0569	4.1	0.97	356.4	14.1	357.7	12.6	365.9	21.9	97.4	18	No CL image
06OH27-4-A	2054	2965	3.3	10.9991	3.7	0.4119	5.3	0.0329	3.7	0.71	208.4	7.7	350.3	15.7	1444.8	71.2	14.4	18	No CL image

4. Results

4.1. Tavan Har Block

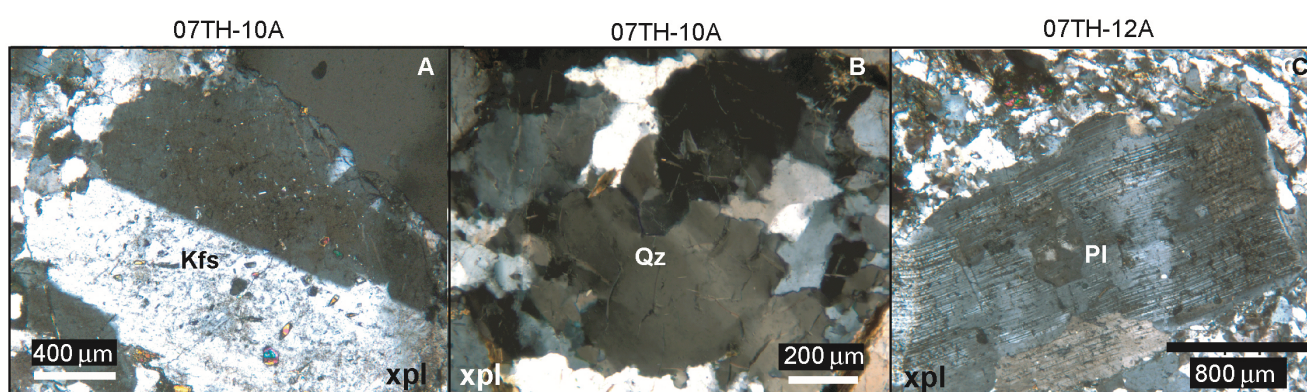
4.1.1. Sample 07TH-10A

4.1.1.1. Microstructural Analysis

Sample 07TH-10A (Figure 3) is an augen gneiss defined in outcrop by pink K-feldspar megacrysts up to a centimeter in length. This sample was taken from the southeastern flank of the sub-region of Tavan Har where greenschist–amphibolite-grade gneisses are mapped (Figure 3). It was collected in the general area where gneissic textures were first identified along a NW-directed transect over the basement high.

The main minerals present in thin section are K-feldspar and plagioclase with smaller amounts of quartz, pyroxene, and biotite. K-feldspar megacrysts commonly exhibit simple-twinning and tartan twinning and contain a number of euhedral to subhedral inclusions. In less deformed regions, K-feldspar grains preserve an elongate rectangular-lath shape (Figure 5A). In more deformed regions K-feldspars exhibit core and mantle structures that commonly include myrmekite. Quartz exhibits amoeboid grain boundaries that are partially recrystallized into smaller grains by subgrain rotation, and bulging recrystallization (Figure 5B). Pyroxene was observed partially altered to biotite.

Figure 5. Photomicrographs, cross polarized light (xpl). Mineral abbreviations follow Whitney and Evans [53]. At Tavan Har, Sample 07TH-10A—(A) simple twinned K-feldspar preserving a primary rectangular shape and euhedral inclusions; (B) Large quartz grains with amoeboid boundaries exhibiting wavy extinction and partially recrystallized by subgrain rotation and bulging; Sample 07TH-12A—(C) Feldspar grain with deformation twins, preserving a primary rectangular shape.



4.1.1.2. U-Pb Geochronology

Zircons from 07TH-10A range in morphology from round to euhedral, equant to needle-shaped, and exhibit oscillatory zoning, mottled, and simple core-rim internal textures, as revealed by CL imaging. Out of all analyses ($n = 45$), we obtained 34 concordant ages, some of which represent core and rim ages on the same grain (Table 1; Figure 6). Concordant ages range from 298 ± 20 to 370 ± 13 Ma (1σ). Aided by zircon morphology and zonation, we identified two age populations. One age population

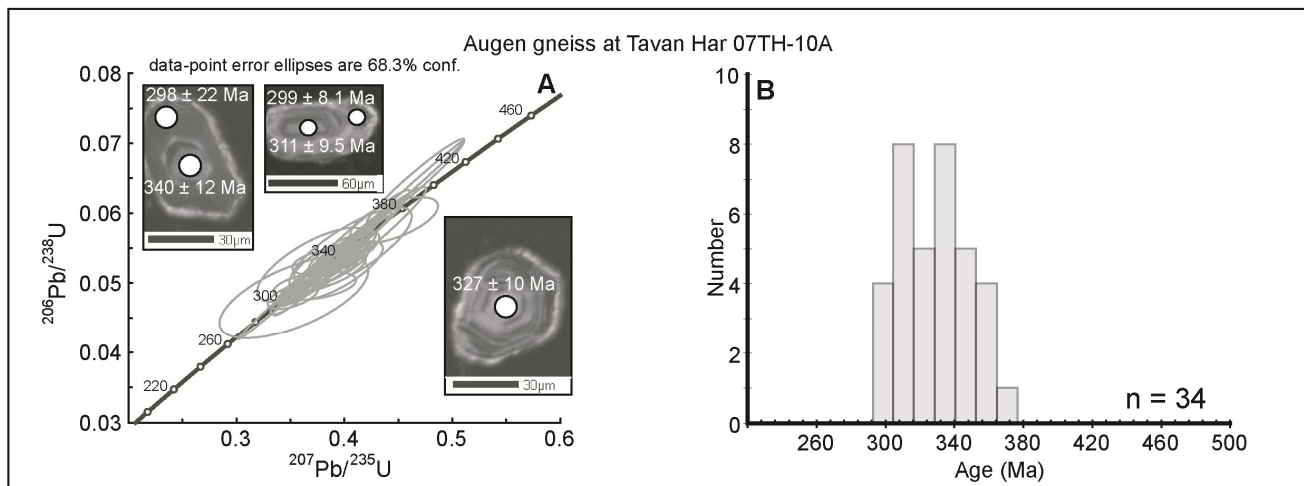
consists of rims with distinctly younger ages than cores and single zircon grains that are mainly equant-shaped and lack oscillatory zoning. U-Pb analyses of this population yield a weighted mean age of 307 ± 6 Ma (2σ), mean square weighted deviation (MSWD) = 0.55, for a total of six concordant analyses (six grains). For these zircons, uranium concentrations range from 791 to 97 ppm. All other analyses (28 in total) gave older ages for zircons that vary in morphology and degree of zonation but that are commonly more elongate and show oscillatory zoning. Combined, analyses of these zircons yield an Age Pick weighted mean age of 331 ± 5 Ma (2σ), MSWD = 1.7 and uranium concentrations that range from 814 to 84 ppm. U/Th ratios for all analyses ranged from 0.7 to 3.0, which is generally characteristic of igneous zircons [54].

4.1.1.3. Interpretation

Sample 07TH-10A (augen gneiss) exhibits microstructural evidence in both quartz and feldspar for crystal plastic deformation at temperatures approaching 600 °C with an extensive overprint of deformation at progressively lower-temperatures and into the brittle regime. Primary textures are nearly obliterated by recrystallization. The only remaining primary microstructures are partially recrystallized elongate/rectangular simple-twinned feldspar laths that contain poikilitic euhedral inclusions and relict outlines of large quartz grains which have been subsequently recrystallized, both suggesting an igneous protolith.

Sample 07TH-10A contains mainly *ca.* 330 Ma age zircons with a few younger ages (ages *ca.* 307 Ma) constrained primarily from zircon rims and equant, unzoned grains. An igneous origin is supported by both zircon morphology and chemistry. These zircon characteristics combined with the identification of primary igneous microstructures, strongly suggest that sample 07TH-10A has an igneous protolith that crystallized during the early Carboniferous (331 Ma) and was later modified during the late Carboniferous (307 Ma).

Figure 6. U-Pb results for 07TH-10A. (A) Concordia plot with cathodoluminescence (CL) images draped over secondary electron images with the location of individual analyses for selected grains; and (B) histogram of ages that are <30% discordant and <5% reverse discordant.



4.1.2. Sample 07TH-12A

4.1.2.1. Microstructural Analysis

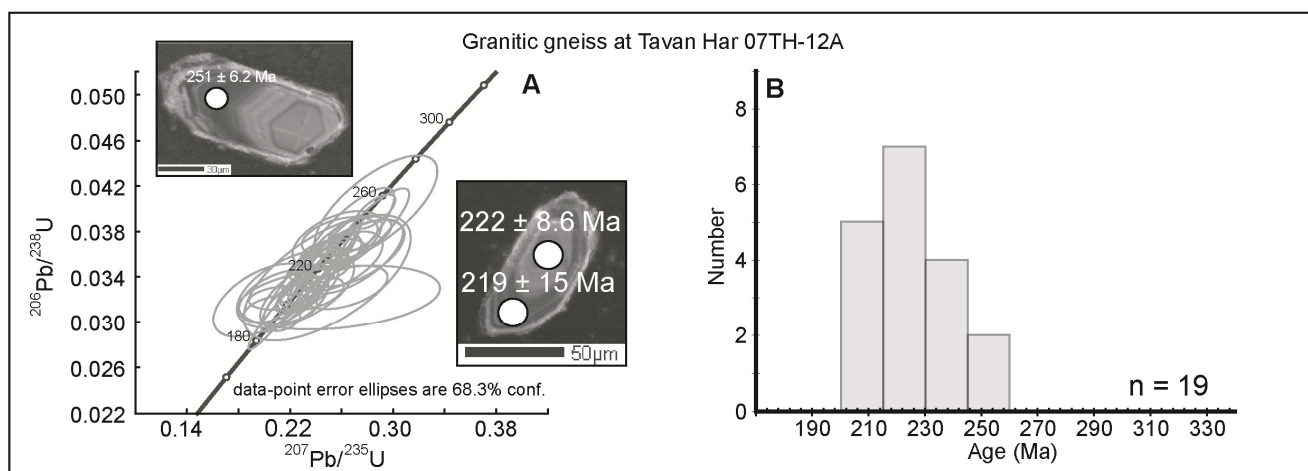
07TH-12A is a sample of quartzo-feldspathic gneiss with a similar mineral composition to 07TH-10A but is finer grained; most K-feldspar grains are less than 1 mm in length, though megacrysts up to 0.5 cm in length were observed. This sample was collected in the center of the subregion of Tavan Har where greenschist-amphibolite grade gneisses are mapped (Figure 3). Sample 07TH-12A was taken within a body of granitic gneiss with a foliation that varies in intensity and orientation. The foliation is stronger near the edges of the body where it is in contact with tectonites and concordant with the shear zone foliation.

In thin section, 07TH-12A is mainly composed of K-feldspar and plagioclase with smaller amounts of quartz, biotite, and amphibole. K-feldspars commonly exhibit both simple and tartan twinning and are fractured. Feldspars exhibit variable degrees of recrystallization with some megacrysts exhibiting core and mantle structures that include myrmekite, whereas others preserve a nearly euhedral shape with only minor recrystallization (Figure 5C). Plagioclase commonly exhibits deformation twins. Quartz, where present, forms ribbons with subgrains that show undulose extinction. Quartz ribbon grain boundaries are commonly mantled by grains formed by bulging recrystallization.

4.1.2.2. U-Pb Geochronology

Sample 07TH-12A yielded subhedral to euhedral zircons that commonly show oscillatory zonation. Nineteen analyses yielded concordant ages that range from 202 ± 9 to 253 ± 19 Ma (1σ). Uranium concentrations ranges from 862 to 60 ppm (Table 2) and U/Th ratios (0.9–2.7) are generally characteristic of igneous zircons [54]. Seventeen analyses from sixteen grains (two analyses were on the core and rim of the same grain) gave concordant ages yielding an Age Pick weighted mean age of 220 ± 6 (2σ), MSWD = 2.3 (Figure 7), the remaining two grains yielded older ages (~ 250 Ma).

Figure 7. U-Pb results for 07TH-12A. (A) Concordia plot with CL images draped over secondary electron images with the location of individual analyses for selected grains; and (B) histogram of ages that are <30% discordant and <5% reverse discordant.



4.1.2.3. Interpretation

Sample 07TH-12A (quartzo-feldspathic gneiss), like 07TH-10A, is extensively recrystallized with quartz and feldspar showing evidence of crystal plastic deformation at temperatures approaching 600 °C followed by progressively lower temperature deformation into the brittle regime. Deformation fabrics characteristic of temperatures <400 °C are dominant. Some primary feldspar microstructures are preserved: Euhedral rectangular feldspar laths were identified; some with simple twinning, others with tartan twinning, which commonly form during and subsequent to crystallization from a melt [55].

Sample 07TH-12A yielded zircons with morphologies (including oscillatory zoning and euhedral grain shapes) and chemistries (U/Th ratio) that support an igneous protolith. The dominant population of zircon ages, *ca.* 220 Ma, is coincident with the main phase of sinistral shear at Tavan Har [26]. This age, combined with the strong ductile–brittle overprint observed in thin section, indicates that the protolith of sample 07TH-12A was emplaced into an active shear zone. The older *ca.* 250 Ma ages constrained from a few zircons are likely xenocrystic grains, possibly assimilated from nearby Early Triassic migmatites [26].

4.2. Yagan-Onch Hayrhan

4.2.1. Yagan-Onch Hayrhan Sample 08OH-03A

4.2.1.1. Microstructural Analysis

Sample 08OH-03A (Figure 4), an augen gneiss, is mainly composed of K-feldspar with smaller amounts of quartz and biotite present. This sample contains a foliation oriented 105°/14° (dip direction/dip angle) and lineation oriented 055°/08° (trend/plunge). K-feldspar augen reach 1 cm in length and indicate a consistent top-to-the-SW sense of shear in outcrop. This sample was collected in an area where gneissic rocks with a dominant top-to-the-SW sense of shear crop out and is north of a Late Jurassic–Early Cretaceous metamorphic core complex characterized by a top-to-the-SE shear fabric (Figure 4).

In thin section K-feldspar augen show well developed core and mantle structures with fine-grained recrystallized rims. Myrmekite is common both on feldspar augen margins as well as in the matrix, also mainly K-feldspar. Quartz and K-feldspar exhibit bulging microstructures and undulose extinction. The medium-grained matrix has a seriate–polygonal texture (Figure 8A).

4.2.1.2. U-Pb Geochronology

Eleven analyses on zircons in sample 08OH-03A yielded concordant ages that range from 220 ± 30 to 311 ± 9 Ma (1σ). We grouped zircons into subsets on the basis of morphology and uranium concentration. Euhedral to subhedral oscillatory zoned grains, which commonly exhibit a large length to width ratio, contain high uranium concentrations that range from 6729 to 285 ppm (Table 3, Figure 9). U/Th ratios range from 0.3 to 7. Out of 20 analyses of zircons within this subset, six concordant ages (on five grains) were obtained with a weighed mean of 248 ± 6 (2σ) Ma, MSWD = 1.01. In this subset of zircons, as uranium concentration increases the degree of discordance increases systematically

(Figure 9A). This relationship is likely caused by Pb-loss that is associated with metamictization of the zircons' crystalline structure [54,56].

The remaining grains generally exhibit anhedral to subhedral, round, square, and equant habits and much lower uranium concentrations, which ranges from 306 to 51 ppm (Figure 9B). U/Th ratios range from 1.8 to 5.8. Five analyses (on five grains) yielded concordant ages that range from 310 ± 18 (2σ) Ma to 284 ± 10 (2σ) Ma with a weighted mean age of 295 ± 6 (2σ) Ma, MSWD = 3.2. One grain contains a resorbed core with a uranium concentration of 561–723 ppm and a concordant age of 310 ± 45 (2σ) Ma, which is mantled by an overgrowth that is dark in CL and yielded a discordant age and uranium concentrations of 6729 ppm.

Figure 8. Photomicrographs, xpl—cross polarized light, Mineral abbreviations follow Whitney and Evans [53] except Wm = white mica. Sample 08OH-03A—(A) seriate–polygonal texture of the quartz/feldspar matrix, Sample 08OH-04C—(B) Plagioclase with deformation twins, Sample 08OH-04D—(C) C'-S-fabric, note fine-grained biotite along fractures (dark regions) and feldspar augen.

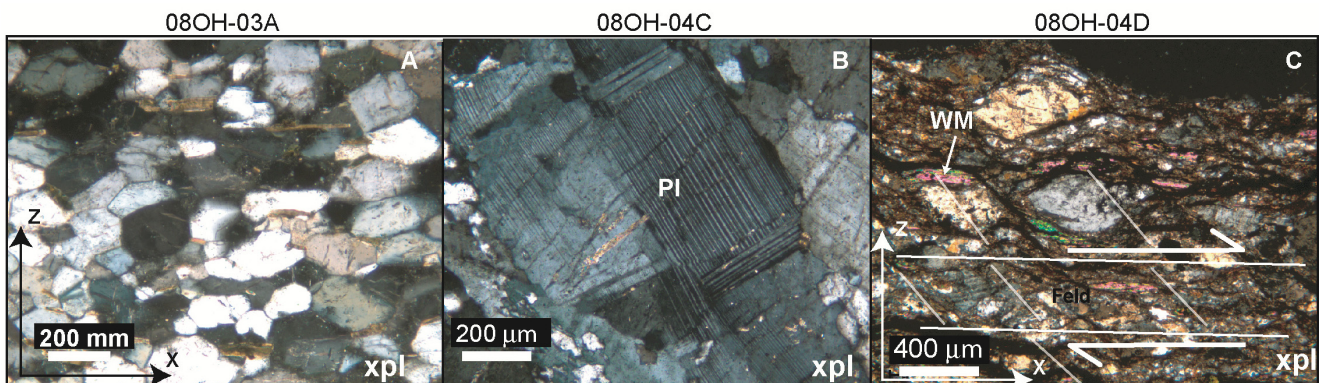
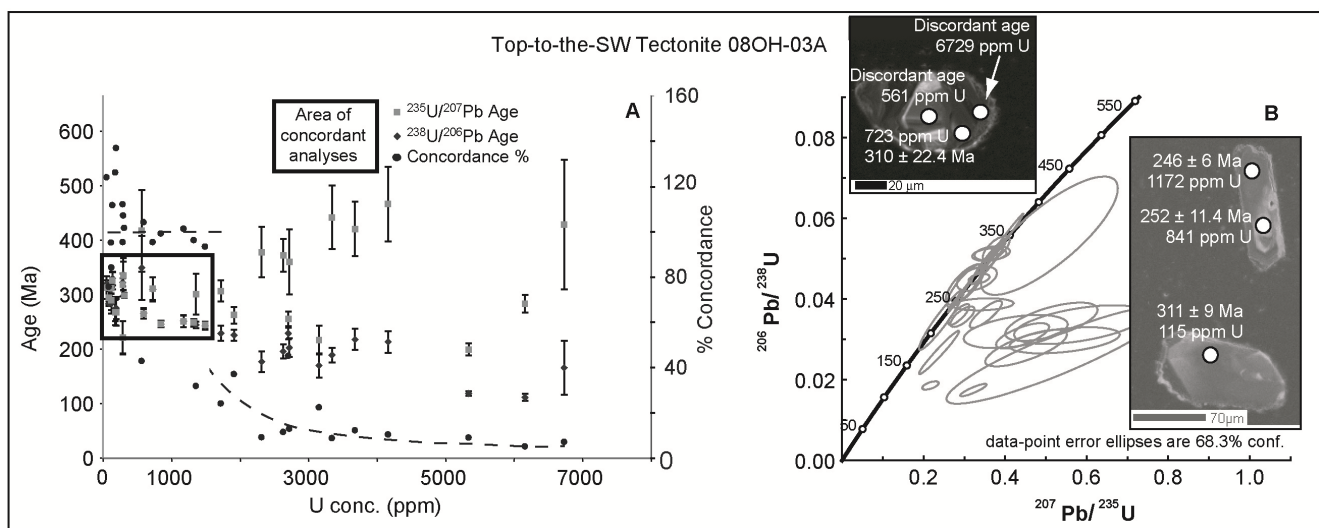


Figure 9. U-Pb results for 08OH-03A. (A) Uranium concentration versus age and % concordance showing the systematic decrease in concordance with increasing uranium concentration and (B) concordia plot with CL images draped over secondary electron images with the location of individual analyses for selected grains.



4.2.1.3. Interpretation

In sample 08OH-03A, an augen gneiss, microstructures observed in thin section are characteristic of crystal plastic deformation at temperatures approaching 600 °C, followed by a period of static recrystallization (evidenced by a seriate–polygonal texture). Minor deformation at temperatures less than 400 °C followed static recrystallization. The K-feldspar megacrysts do not preserve any magmatic features, such as zoning or twinning, but their large size is suggestive of a magmatic origin. Zircon morphology (needle-like grains) and chemistry (U/Th ratios) suggests sample 08OH-03A has an Early Triassic igneous protolith that incorporated Late Carboniferous–Early Permian xenocrystic zircons some of which were mantled by rims when incorporated into the melt.

4.2.2. Yagan-Onch Hayrhan Migmatite, Sample 08OH-04

4.2.2.1. Microstructural Analysis

Sample 08OH-04 was taken from an outcrop of migmatite gneiss. In outcrop the migmatite exhibits a foliation that dips shallowly to the north. In the surrounding region outcrops of granitic gneiss were identified with a shallowly south-dipping foliation and contain asymmetric feldspar augen which give a top-to-the-northeast shear-sense.

Two thin sections were made from sample 08OH-04 (migmatite): one of the leucosome (08OH-04C) and one of the mesosome (08OH-04D). The leucosome is mainly composed of quartz, plagioclase, K-feldspar, and white mica but also contains garnet. Feldspar grains possess multiple twins and deformation twins (Figure 8B), and are commonly associated with myrmekite. Quartz and feldspar contain subgrains and commonly show undulose and wavy extinction. Feldspar grains exhibit bulging recrystallization along their margins. Most mica grains have small reaction rims, some are corroded along their margins. Some mica grains are kinked.

Sample 08OH-04D, the mesosome, contains a foliation dipping 350°/32°. No shear sense indicators were observed in outcrop. This sample is mainly composed of feldspar and biotite with a smaller amount of garnet, white mica, quartz, and allanite. Deformation is pervasive: biotite forms a fine-grained matrix along an anastomosing network of fractures. In thin section white mica fish and a C'-S-fabric give a top-to-the-north shear sense (Figure 8C).

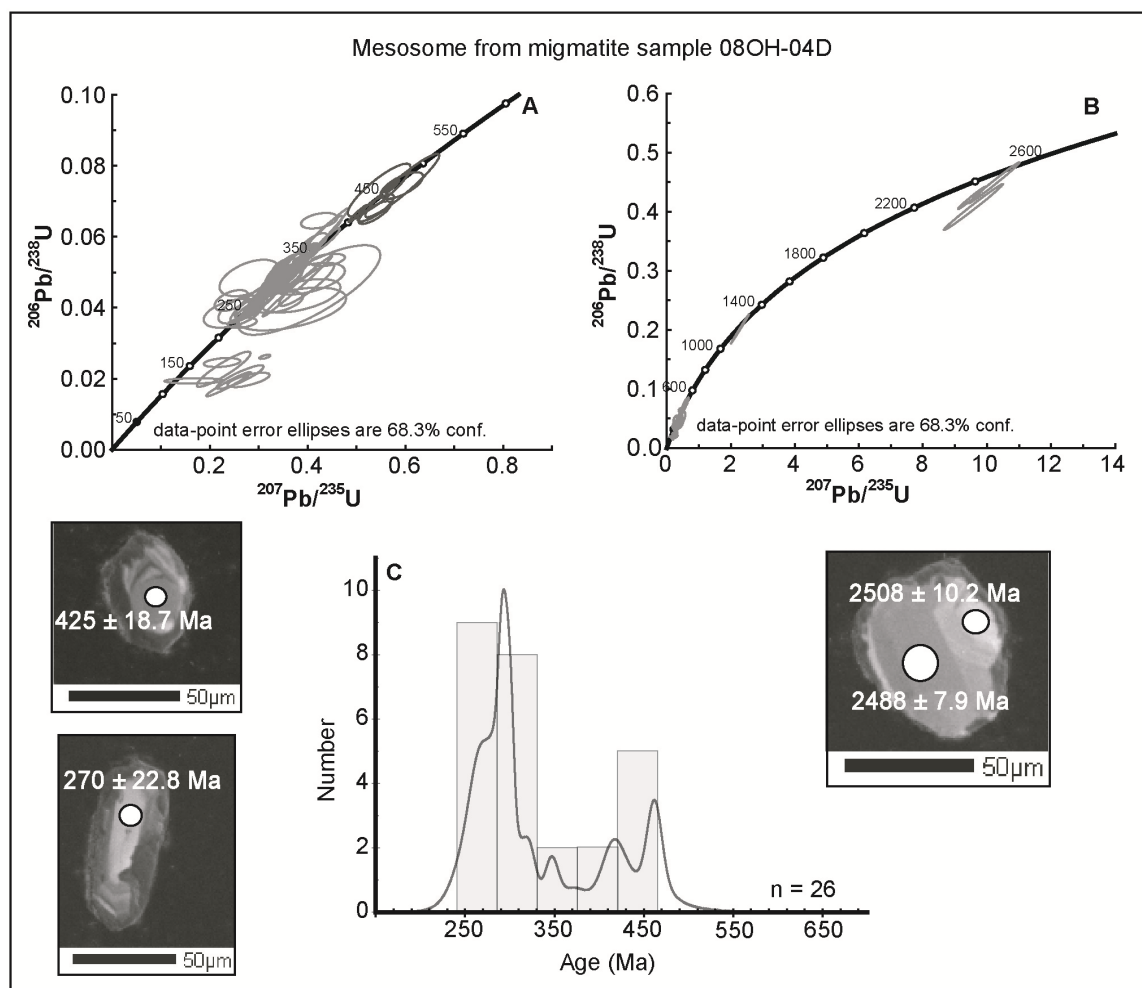
4.2.2.2. U-Pb Geochronology

Only the mesosome (08OH-04D) yielded zircons. These zircons exhibit a range of morphologies including anhedral to euhedral grain-shapes (Figure 10). In total, thirty concordant analyses yielded ages that range from 253 ± 17 to 2560 ± 13 (1 σ) Ma.

CL imaging revealed that many grains have complex internal textures with most containing resorbed cores with overgrowths that are dark. One distinct group of zircons has resorbed cores, some with oscillatory zoning, that are surrounded by rims that are characteristically dark in CL images. Ages range from 2509 ± 10 (1 σ) to 263 ± 21 (1 σ) Ma for nine analyses from nine grains (Table 4, Figure 10). Two grains yielded ~2500 Ma ages, both are round with one showing a core mantled by a thin dark (in CL) rim. Another euhedral grain with a core surrounded by a dark (in CL) rim was dated to 1250 ± 16 Ma (2 σ). Uranium concentrations in resorbed cores range from 725 to 33 ppm; U/Th ratios

range from 6.8 to 0.5. Five grains had wide enough rims for U-Pb analysis, but no concordant ages were obtained, likely a consequence of Pb-loss via radiation damage as the rims have high uranium concentrations that are generally greater than 1500 ppm [54,56]. U/Th ratios for rims are distinct from cores, ranging from 58.2 to 11.6. Rim U/Th values are characteristic of metamorphic zircons [54].

Figure 10. U-Pb results for 08OH-04D. (A) and (B) Concordia plot with CL images draped over secondary electron images with the location of individual analyses for selected grains; (C) Histogram with the relative probability age distribution of Phanerozoic ages that are <30% discordant and <5% reversely discordant.



We identified a second group of zircons on the basis of their needle-shaped morphology or morphology, consistent with being a fragment of a broken needle-shaped grain. CL imaging revealed that this group contains zircons mantled by dark rims and grains where overgrowths are absent. Of nineteen grains analyzed, five yielded concordant ages with a weighted mean age of 272 ± 12 (2σ) Ma, MSWD = 0.9. Uranium concentrations for this group ranges from 1945 to 137 ppm. U/Th ratios range from 8.9 to 0.5. All remaining grains (16 analyses from 12 grains) have highly variable internal textures and morphologies that range from anhedral to euhedral. Six grains yielded concordant ages that range from 267 ± 18 (1σ) to 415 ± 12 (1σ) Ma. An additional fourteen grains were dated from a mount that was not imaged for zircon morphology or zonation. The zircon ages from this group are used in histograms and age-probability plots to compliment the data described above.

When all concordant ages are considered (30 analyses) two distinct Paleozoic age populations are identifiable: A large population at ~300 Ma with a peak skewed toward younger ages (possibly 272 Ma, as reflected in the ages of needle-shaped zircons) and a relatively small age population at 450 Ma (Figure 10B).

4.2.2.3. Interpretation

Both the mesosome and leucosome exhibited evidence of deformation, though it is much more prevalent in the mesosome. The leucosome appears undeformed in outcrop but shows evidence in thin section for deformation at temperatures approaching 600 °C which is overprinted by lower temperature deformation fabrics (<400 °C). The mesosome is highly deformed at temperatures ≤ 400 °C with an extensive brittle overprint, obscuring any evidence of deformation at higher temperatures. The low-temperature deformation fabrics record a top-to-the-north sense of shear, which has been previously observed at a few locations at Yagan-Onch Hayrhan but is not a common regional structural trend [29].

Though no primary microstructures were identified in thin section from the mesosome, the U-Pb zircon age distribution (with a wide range of core ages spanning approximately 2500–263 Ma) is highly suggestive of a sedimentary protolith. Moreover, the older Precambrian and early Paleozoic-age grains and cores tend to be more rounded and fractured than the more abundant younger late Paleozoic-age grains, consistent with the older grains having experienced a longer, more protracted history, possibly including weathering and transport at the Earth's surface.

The zircon age populations in 08OH-04D are strikingly similar to age populations constrained from Permian sandstone samples collected from the region surrounding Yagan-Onch Hayrhan that were presented in a combined detrital zircon/basin analysis study by Heumann *et al.* [43]. The work of Heumann *et al.* contained age populations between ~262–295 Ma, ~420–500 Ma, and zircons as old as ~2500 Ma [43]; whereas our study constrained zircon populations at ~270–300 Ma and ~450 Ma and sampled Precambrian grains with ages of ~1250 Ma and ~2500 Ma. We cannot make a more quantitative comparison of the relative age distributions because our study used a zircon sampling strategy of selecting only inclusion-free zircons, which contrasts with the sampling strategy of Heumann *et al.* [43], which did not exclude zircons due to the presence of inclusions. A Permian protolith is also consistent with previous work that documented a gradual transition from undeformed Permian sedimentary rocks to greenschist-grade metasediments at Yagan-Onch Hayrhan in the region surrounding the metamorphic core complex [29].

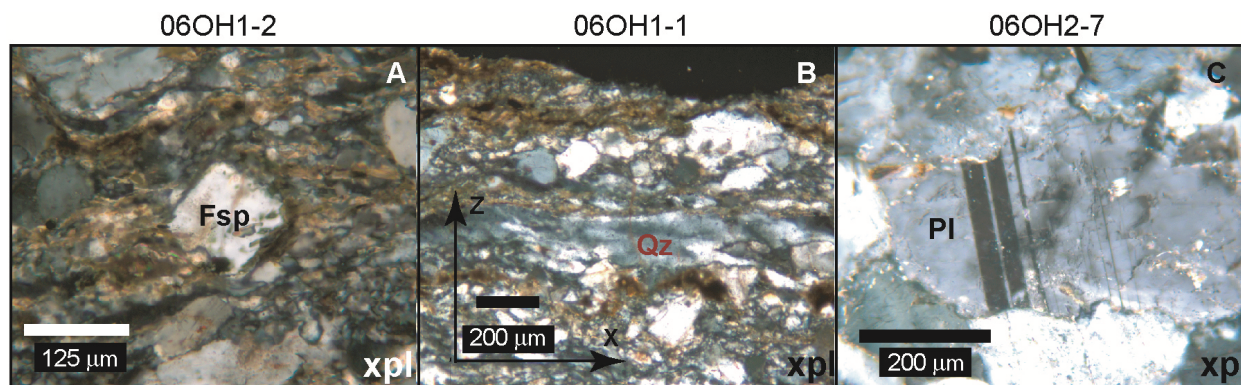
4.2.3. Sample 06OH1-2

4.2.3.1. Microstructural Analysis

Sample 06OH1-2 is an augen gneiss collected from the lower plate of the Late Jurassic–Early Cretaceous Yagan-Onch Hayrhan metamorphic core complex (Figure 4). It is many composed of quartz and feldspar with minor amphibole and alteration products such as chlorite. This sample contains a foliation that dips 353°/31° and a stretching lineation oriented 357°/30°. In outcrop, feldspar augen are common, reaching ~0.5 cm in length, and exhibit σ -clast asymmetry that give a top-to-the-S sense of shear. Sample 06OH1-2 possesses a foliation defined by compositional bands of quartz and

feldspar, alternating with bands of biotite and amphibole. In thin section quartz + feldspar and mica + amphibole bands form a C'-S fabric that confirms a top-to-the-S sense of shear. Feldspar and amphibole grains are common and are generally surrounded by a recrystallized matrix. In regions of low strain, feldspars retain a primary subhedral rectangle or square-shape (Figure 11A). In regions of high strain, feldspars show core and mantle structures, exhibit undulose extinction, deformation twinning, and have myrmekite developed along their margins. Amphiboles are commonly fractured and altered to chlorite. Quartz is extensively deformed, forming ribbons with subgrains, which have wavy-undulose extinction. Quartz ribbons exhibit subgrain rotation and bulging microstructures and contain brittle fractures.

Figure 11. Photomicrographs, xpl-cross polarized light. Mineral abbreviations follow Whitney and Evans [53]. Sample 06OH1-2—(A) feldspar exhibiting a primary square shape; Sample 06OH1-1—(B) relict quartz ribbon surrounded by quartz exhibiting lower temperature deformation microstructures; Sample 06OH2-7—(C) partially recrystallized plagioclase grain that exhibits primary magmatic twinning.



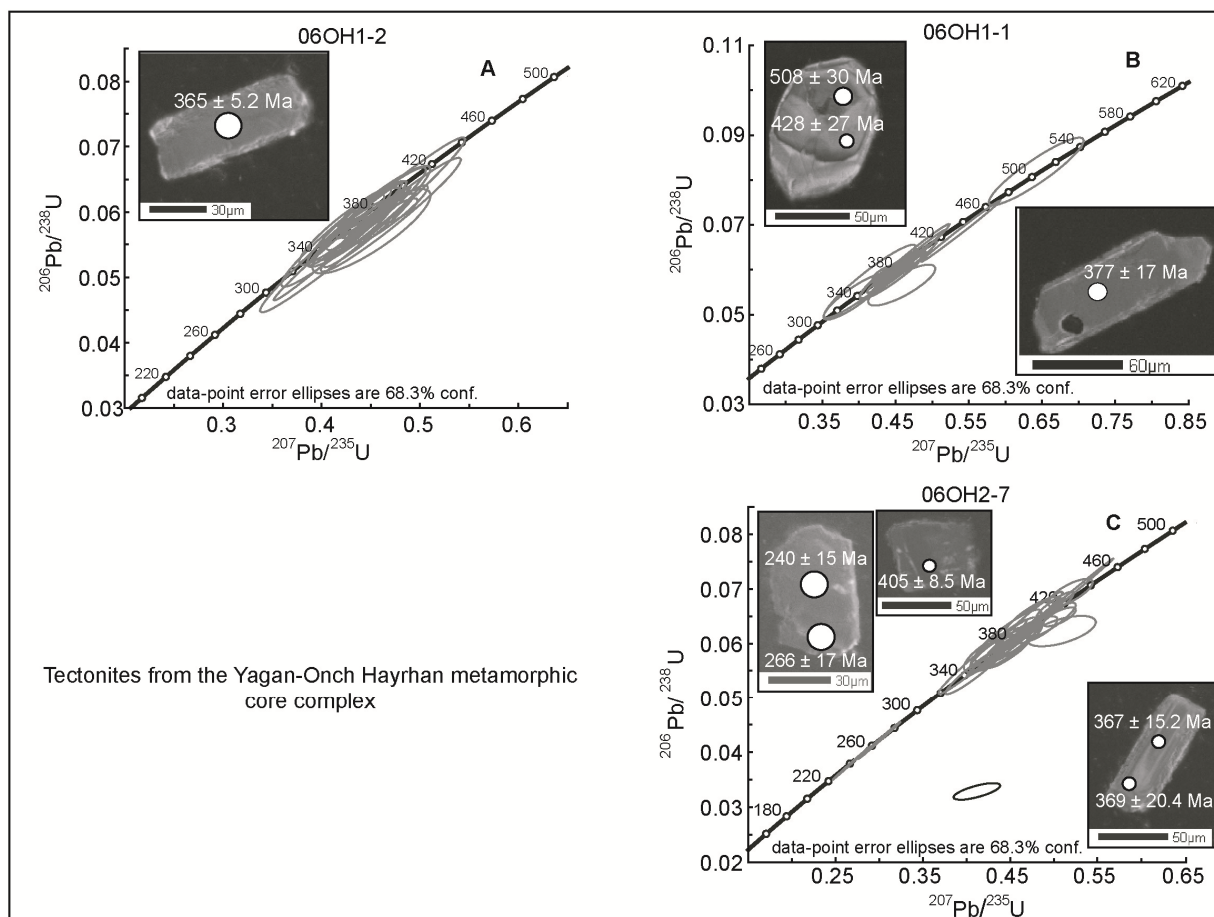
4.2.3.2. U-Pb Geochronology

Sample 06OH1-2 yielded mainly subhedral zircons that are commonly broken into rectangle and square-shaped fragments. CL imaging revealed that some grains exhibit weak oscillatory zoning (Table 5, Figure 12A). Eighteen analyses yielded concordant ages that range from 341 ± 32 to 379 ± 25 Ma (1σ). Eighteen analyses gave an Age Pick weighted mean age of 367 ± 9 Ma (2σ), MSWD = 0.3, with U/Th ratios that range from 2.0 to 4.3 and uranium concentrations that range from 152 to 545 ppm.

4.2.3.3. Interpretation

In sample 06OH1-2 crystal plastic deformation of feldspar and quartz and fracturing of amphibole provide evidence of deformation at temperatures between 600 and 700 °C, which is overprinted by deformation at lower temperatures (< 400 °C); associated with the alteration of amphibole to chlorite and continued crystal plastic deformation of quartz and feldspar. The C'-S fabric indicates that most of the deformation took place during top-to-the-S shear which is consistent with the regional deformation fabric associated with formation of the metamorphic core complex. In lower strain areas, feldspar grains preserve rectangle- or square-shapes, suggesting an igneous protolith. The presence of primary igneous microstructures and a single population of zircons suggest sample 06OH1-2 has an igneous protolith which crystallized during the Late Devonian.

Figure 12. U-Pb results for samples collected from the lower plate of the Yagan-Onch Hayrhan metamorphic core complex. Concordia plots with CL images draped over secondary electron images with the location of individual analyses for selected grains from (A) 06OH1-2, (B) 06OH1-1, and (C) 06OH2-7. Strongly discordant ages are presented in black. All other analyses are presented in light gray.



4.2.4. Sample 06OH1-1

4.2.4.1. Microstructural Analysis

Sample 06OH1-1 is a cataclastically deformed mylonite, also collected from the lower plate of the Late Jurassic–Early Cretaceous Yagan-Onch Hayrhan metamorphic core complex. This sample is a gray fine-grained mylonite composed mainly of quartz and feldspar with smaller amounts of white mica, garnet, and products of alteration such as chlorite and sericite. The sample contains a foliation that dips $305^\circ/28^\circ$ and a lineation oriented $333^\circ/24^\circ$. In thin section sample 06OH1-1 exhibits a C'-S fabric, asymmetric feldspar porphyroclasts, and mica fish that give a top-to-the-SE shear sense. Fabric analysis also identified relict quartz ribbons as well as feldspar grains that form core and mantle structures with myrmekite developed along their margins. Quartz ribbons have subgrains and show recrystallization along grain margins by subgrain rotation and bulging (Figure 11B). Undulose extinction is common in both relict and recrystallized quartz grains. Feldspars and garnets are fractured and microfaulted, with some fractures/faults filled with sericite and chlorite. Chlorite was observed replacing garnet, including a chlorite pseudomorph after garnet.

4.2.4.2. U-Pb Geochronology

Sample 06OH1-1 yielded mainly subhedral zircons that are commonly broken into rectangle- and square-shaped fragments (Figure 12B). CL imaging revealed some grains contain weak oscillatory zoning. Eighteen analyses yielded concordant ages ranging from 339 ± 20 to 508 ± 30 Ma (1σ). Sixteen analyses yield a combined Age Pick mean age of 373 ± 8 Ma (2σ), MSWD = 0.9. U/Th ratios range from 1.2 to 3.0, generally characteristic of igneous zircons, and uranium concentrations vary from 2183 to 147 ppm with all but one analysis below 350 ppm (Table 6).

4.2.4.3. Interpretation

Sample 06OH1-1 (cataclastically deformed mylonite) exhibits evidence of garnet growth during or prior to the onset of deformation. Feldspar and quartz show evidence of deformation at temperatures approaching 600 °C. The dominant fabrics record deformation at lower temperatures (400–200 °C) with a pervasive brittle overprint. Low-grade deformation was associated with significant alteration of garnet as evidenced by a chlorite pseudomorph after garnet. The C'-S fabric indicates that most of the deformation recorded by the microstructures described above formed during top-to-the-SE shear associated with core complex formation. U-Pb analysis of zircons from 06OH1-1 yielded a single age population with a mean age of 373 ± 8 (2σ) Ma. This single age population may reflect the timing of crystallization of an igneous rock or locally sourced zircons in a sedimentary rock.

The similarity between zircon morphology and the weighted mean ages for 06OH1-1 and 06OH1-2 suggests congruence between the datasets from the two samples. This is further supported by petrographic observations that show both samples share a similar mineral assemblage, differing mainly in grain size and degree of alteration. Therefore, we favor an igneous protolith for both samples. Combined, their Age Pick mean age is 371 ± 10 Ma (2σ), MSWD = 0.6, $n = 34$.

4.2.5. Sample 06OH2-7

4.2.5.1. Microstructural Analysis

Sample 06OH2-7, a foliated gneiss with a strong intersection lineation, was collected approximately 3 km to the southeast of 06OH1-2. Like the two previous samples of mylonite and augen gneiss, it is characterized by a strong foliation dipping $028^\circ/30^\circ$ that is defined by alternating pink quartz + feldspar bands and gray biotite + amphibole bands. An intersection lineation was observed oriented roughly $106^\circ/24^\circ$. In thin section, plagioclase grains commonly show multiple twinning and are recrystallized to varying degrees (Figure 11C). All minerals are highly deformed; feldspars exhibit deformation twins and are mantled by myrmekite, with some grains forming core and mantle structures. Large quartz grains are commonly partially recrystallized by subgrain rotation and bulging. Recrystallized grains show undulose extinction. Amphibole was observed partially replaced by biotite.

4.2.5.2. U-Pb Geochronology

Sample 06OH2-7 yielded zircons with a range of morphologies, including equant, stubby, and fragmented needle-shaped grains (Figure 12C). Through CL imaging we identified both unzoned and

oscillatory zoned grains. Nineteen analyses yielded concordant ages that range from 240 ± 15 to 405 ± 9 Ma (1σ). U-Pb ages correlate with internal texture; six analyses on five oscillatory zoned grains give a weighted mean age of 368 ± 14 Ma (2σ), MSWD = 0.6. Of the remaining nine unzoned grains, eight yield a weighted mean age of 393 ± 8.7 Ma, MSWD = 0.9. Two analyses on one unzoned grain yield a weighted mean age of 252 ± 22 Ma (2σ ; MSWD = 1.3), and an average U/Th ratio of 91.3, distinctly higher than all other analyses (1.4–3.7) and characteristic of metamorphic zircon (Table 7, Figure 12C) [54]. Interpretation of two analyses from one grain is not statistically robust and warrants further justification [47]. However when additional regional data is considered, the identification of this age may be significant. *Ca.* 250 Ma zircons are common in other samples from Onch Hayhran (specifically sample 08OH-03A) and Tavan Har (07TH-12A) and in addition to the data of our study, other studies have identified similar ages from Tavan Har (Webb *et al.* [26]) and Bulgan Uul (~60 km from Onch Hayhran; Heumann *et al.* [43]). An additional three grains not imaged yielded concordant ages. These grains range in age from 356 ± 14 to 368 ± 3.8 Ma, which are within the range of ages constrained for oscillatory zoned grains.

4.2.5.3. Interpretation

Sample 06OH2-7 exhibits microstructures that are characteristic of initial deformation at relatively high temperatures (near 600 °C) transitioning to deformation at 400 °C and progressively lower-temperature conditions. Low-grade deformation was associated with alteration of amphibole to biotite. This sample generally does not contain the extensive brittle overprint observed in the other two samples from the metamorphic core complex (06OH1-1 and 06OH1-2). Sample 06OH2-7 preserves plagioclase grains which have magmatic twins that suggest an igneous protolith.

Like samples 06OH1-1 and 06OH1-2, both the microstructure and U-Pb results for sample 06OH2-7 suggest an igneous protolith which formed during the Late Devonian (*ca.* 368 Ma). However, in sample 06OH2-7, U-Pb zircon results also suggest that the protolith assimilated older Early Devonian xenocrystic zircons (*ca.* 393 Ma), and was later metamorphosed at *ca.* 250 Ma.

5. Tectonic Significance and Implications for the Existence of Precambrian Basement

5.1. Devonian Protoliths

All three samples collected from the lower plate of the Yagan-Onch Hayrhan metamorphic core complex (06OH1-2; 06OH1-1; 06OH2-7) have Late Devonian igneous protoliths. Southern Mongolia was the site of an active arc above a north-dipping subduction zone during the latest Silurian–late Carboniferous—the South Mongolia arc [3,4,20,38,42,57–60]; therefore the protoliths of these samples are likely arc-derived igneous rocks.

Devonian volcanic rocks are present to the north and west of Yagan-Onch Hayrhan, near the town of Nomgon (Figure 2) [19]. Our results imply that the Yagan-Onch Hayrhan region is underlain by Devonian igneous rocks that were subsequently metamorphosed, possibly at *ca.* 250 Ma, then exhumed within the lower plate of the Yagan-Onch Hayrhan metamorphic core complex during the Late Jurassic–Early Cretaceous. Accordingly, these samples may provide a window into the basement

underlying much of the Yagan-Onch Hayrhan region, into which Permian–Triassic plutons were emplaced and over which Permian and younger sediments were deposited (see following sections).

5.2. Carboniferous Protolith

Sample 07TH-10A, the augen gneiss from Tavan Har with an igneous protolith, likely formed during Carboniferous magmatism within the South Mongolia arc. Undeformed Carboniferous igneous rocks (some dated at *ca.* 330 Ma) which record arc magmatism are present throughout southeastern Mongolia [23,38,39,43,60,61]. Moreover, provenance work on the Permian strata of southeastern Mongolia identified Carboniferous arc lithologies as a dominant provenance [43]; further demonstrating the regional extent of arc magmatism during the Carboniferous.

In southeastern Mongolia Carboniferous volcanic rocks are mainly intermediate to mafic lava flow and ash deposits [23,61]. Plutonic rocks dated at *ca.* 330 Ma in southeastern Mongolia are generally more felsic than volcanic rocks of the same age, consisting of granodiorites, monzonites, and quartz monzonites, which have been dated within the Saykhandulaan and Mandakh inliers [39], just northeast of Tavan Har (Figure 2), but are likely more widespread as many plutons within southeastern Mongolia lack isotopic age control.

5.3. Permian–Triassic Protoliths

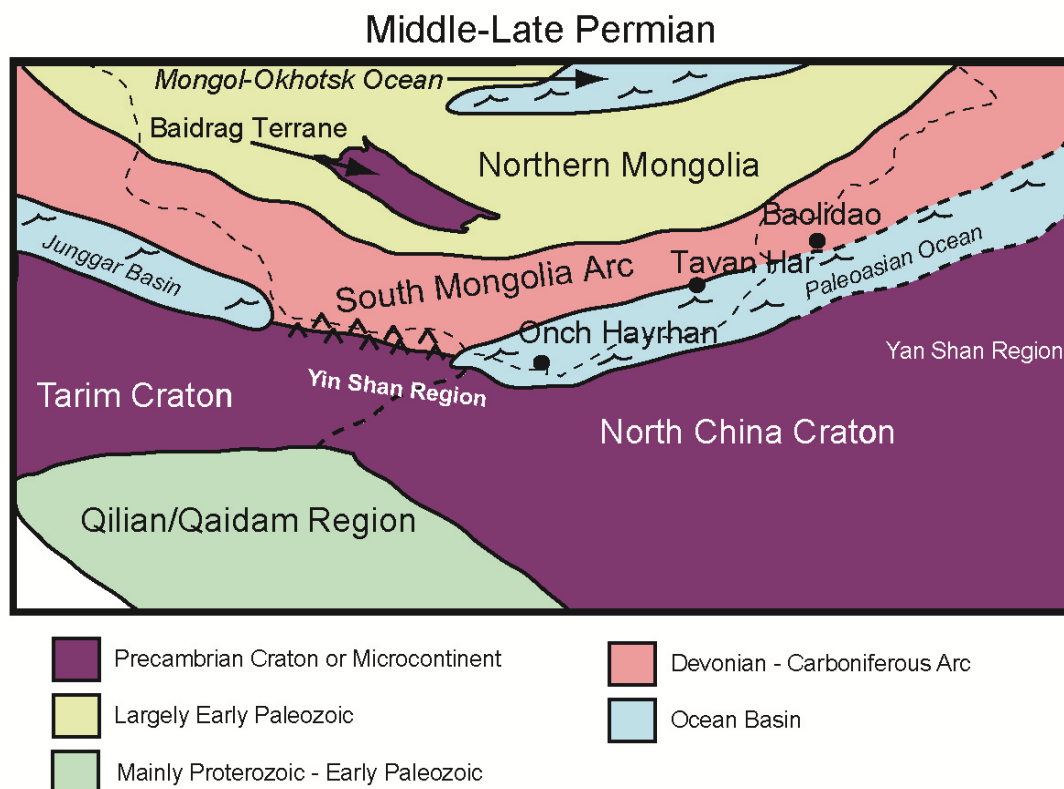
Two samples analyzed have latest Permian–Triassic igneous protoliths. The protolith to 08OH-03A, an augen gneiss with a top-to-the-SW fabric, was emplaced at *ca.* 250 Ma. Sample 07TH-12A, a quartzo-feldspathic gneiss, was emplaced at *ca.* 220 Ma. Magmatism was common during the Late Permian–Late Triassic, as evidenced by *ca.* 290 Ma and 250–225 Ma plutons and volcanic rocks that are now exposed at the surface in Mongolia and northern China [23,39,59–66]. This igneous activity occurred during and into the waning stages of collision between southern Mongolia and northern China [62–66].

Our work is only one of a number of recent studies that document latest Permian–Middle Triassic magmatism in the broader region surrounding southeastern Mongolia. Granitoids, with varying amounts of syn-to-post intrusional deformation, have been identified in adjacent portions of China just north of the Yan Shan deformation belt and east of Tavan Har. Zhang *et al.* [66] identified granitoids that gave U-Pb zircon SHRIMP ages of 254 ± 4 Ma, 241 ± 2 Ma, and 237 ± 1 Ma (all errors are 2σ). The oldest intrusion has a locally developed foliation along one of its boundaries, whereas the second two are not deformed. In closer proximity to southeastern Mongolia, the late Carboniferous Baolidao arc mafic to intermediate magmatic suite is intruded by the 234 ± 7 Ma (2σ) Halatu granitoids (Baolidao in Figure 13) [62,63]. Where studied by Chen *et al.* [63], the Baolidao rocks are pervasively deformed, but the Halatu granitoids show no signs of deformation. In the lower plate of the Yagan-Onch Hayrhan metamorphic core complex Wang *et al.* [65] identified a set of granitoids with a U-Pb zircon TIMS age of 228 ± 7 Ma (2σ).

The varying degree of deformation in the latest Permian–Middle Triassic granitoids suggest emplacement within a complex tectonic setting. Extensional collapse during delamination of overthickened lithosphere has been proposed for the formation of many of these granitoids [64]. The possible surface manifestation of this extension, a Late Triassic (possibly *ca.* 224–208 Ma) metamorphic core complex,

was identified along the North China Craton–South Mongolia arc suture zone that deforms both the Baolidao and Halatu plutonic rocks (discussed above) in its lower plate [67].

Figure 13. Middle–Late Permian tectonic setting of southern Mongolia. Yagan-Onch Hayrhan and Tavan Har were located within the Paleasian Ocean between the subareal portion of the South Mongolian arc and the North China and Tarim cratons. During the Late Permian–Early Triassic, the Paleasian Ocean progressively closed resulting in collision between northern China and the South Mongolia arc. After Johnson *et al.* [37].



As shown by Webb *et al.* [26] and now further supported by our results, Triassic igneous activity was not restricted to the suture zone, but extended many 100's of kilometers into southeastern Mongolia where the protoliths of samples 07OH-03A (an augen gneiss) and 07TH-12A (a quartzo-feldspathic gneiss) were emplaced at ~250 and ~220 Ma, respectively. In particular, 07TH-12A was synkinematic with sinistral shear in the EGFZ. This sinistral shear zone was a significant regional feature with ~170 km of constrained Triassic left-lateral offset [30,31] and overprints an earlier partial melting event older than *ca.* 240 Ma [26].

When all available work in both northern China and southern Mongolia is considered, a complex latest-Permian–Triassic tectonic setting emerges in which extension, plutonism, and intraplate sinistral shear were active. This setting reflects the complex nature of collision zones and associated intracontinental deformation zones and may be analogous to parts of present day Tibet [13,68].

Sample 08OH-04D (migmatite, mesosome) is the only sample examined with a sedimentary protolith. We suggest that the protolith to 08OH-04D is equivalent to the Permian strata ubiquitous in southeastern Mongolia. Analysis of cores of zircons from 08OH-04D yielded ~300 Ma and ~450 Ma age populations and a few much older Precambrian ages (~2500 and ~1250 Ma). As stated previously,

these age populations are similar to those constrained from detrital zircons from Permian strata in southeastern Mongolia by Heumann *et al.* [43]; the depositional setting of which can provide important constraints on the provenance of these grains.

Johnson *et al.* [37] and Heumann *et al.* [43] presented results from extensive field studies of Permian strata in southern Mongolia. These strata were deposited from a northwesterly source region into a sedimentary basin during collision between the North China/Tarim cratons and the South Mongolia arc (Figure 13). The dominant source for sediment was identified as the then-extinct South Mongolia Paleozoic arc(s) with minor contributions from the North China craton and associated accreted terranes (such as the Qilian and Qaidam) along the northern margin of the North China craton [43]. With respect to the Precambrian age zircons identified in our study, *ca.* 2500 Ma zircons are common in the North China and Tarim cratons and *ca.* 1250 Ma zircons are common in the Tarim craton and within the accreted terranes found along the margin of the North China craton, consistent with input from northern China [69–79].

After deposition during the Permian, sample 08OH-04D (migmatite mesosome) experienced high-temperature deformation and metamorphism, resulting in dissolution of zircon grains forming resorbed cores and growth of new zircon as overgrowths and new zircon grains with extremely high uranium concentrations. Metamorphism occurred at or soon after ~ 265 Ma—the age of the youngest core mantled by a high-uranium concentration rim. The metamorphic zircon with an age of ~ 250 Ma, dated in sample 06OH2-7 (tectonite with a Late Devonian igneous protolith) may have formed at the same time as the overgrowths observed in sample 08OH-04D, as both are associated with high uranium concentrations (> 1000 ppm), U/Th ratios indicative of metamorphic zircon, and were sampled from sites located in close proximity (~ 12 km apart). This would place a *ca.* 252 ± 22 (2σ) Ma age on metamorphism in both samples, coinciding with the waning stages of collision between the northern China and the South Mongolia arc and synchronous with the intrusion of the protolith to 08OH-03A (248 ± 6.4 Ma, 2σ). However, more concordant ages are needed to confirm this age of metamorphism for sample 08OH-04D. The timing of emplacement of the felsic intrusions that surround the migmatite outcrop sampled and possibly sourced the leucosome was not constrained because the leucosome did not yield any zircons. However, these intrusions may also be Triassic in age, given the abundance of deformed Triassic igneous rocks documented at Yagan-Onch Hayrhan, as shown by our work (see above) and the work of Wang *et al.* [65] who identified deformed Triassic plutons (*ca.* 228 ± 7 Ma, 2σ) in the lower plate of the Yagan-Onch Hayrhan metamorphic core complex. A *ca.* 250–230 Ma age for the felsic intrusions that surround sample 08OH-04 would place the timing of intrusion soon after deposition of the protolith of sample 08OH-04D and would be nearly coeval with the suspected timing of metamorphism.

6. Tectonic Implications and Summary

In light of the discussion above, Precambrian basement in southeastern Mongolia is not required to explain the few Precambrian zircons found in sample 08OH-04D (migmatite mesosome) of our study or zircon ages from other studies that sampled basement in the same region [9,10] which likely also dated Precambrian zircons from sedimentary protoliths. The Precambrian zircons found in southeastern Mongolia were most likely sourced by the Tarim craton and the North China craton and

associated accreted terranes (such as in the Qilian, Qaidam, Yin Shan and Yan Shan regions) located along the north China margin [69–79].

Consequently, we find no evidence to support the existence of the Precambrian Totoshan-Ulanuul or Tsagaan-Khairkhan blocks, which represent a substantial portion of the South Gobi Microcontinent. Instead, the basement of southeastern Mongolia is composed of highly deformed metaigneous and metasedimentary rocks formed within the Devonian–Carboniferous South Mongolia arc and during its subsequent Permian–Triassic collision with northern China.

The absence of large swaths of Precambrian basement underlying southeastern Mongolia has profound implications for both the tectonic history of the CAOBS as well as the partitioning of subsequent intraplate deformation. Our results indicate that models which describe the tectonic history of the southeastern Mongolia portion of the CAOBS do not have to explain the origin, position, and movement through time of a Precambrian basement-cored microcontinent. Instead this portion of the South Mongolia arc formed along the southern margin of northern Mongolia.

This heterogeneous, highly deformed basement can be considered rheologically weak when compared to adjacent regions of cratonic and microcontinent crust (*i.e.*, northern Mongolia and northern China). This weak nature is exemplified by the presence of extensive Permian–Triassic deformation. We have documented extensive Permian–Triassic deformation and plutonism within the suture zone extending northward into southern Mongolia during the waning stages of collision, indicating that southern Mongolia experienced a large degree of collisional strain. Furthermore, a heterogeneous, multiply deformed and metamorphosed crust can explain why southeastern Mongolia has served as a locus for subsequent Mesozoic–Cenozoic intraplate deformation, which has included phases of shortening [27,33,44,80–83] extension [25,29,32,33,44,82–85], and strike-slip deformation [24,26,28,33,82–85].

Acknowledgments

This work was supported by National Science Foundation grant numbers EAR-4360537165 and EAR-0929902 to L. Webb, and EAR-0537318 to C. Johnson. We thank Ian Semple, Bolor Minjin, Chuluun Minjin, G. Sersmaa, U. Jalbaa, M. Ganbai, and N. Manchuk for their contributions during three field expeditions to southeastern Mongolia as well as Michael Cheatham, Jack Hietpas, and Aaron Satkoski for their help preparing zircon mounts and with zircon imaging. George Gehrels and his fellow members of the Arizona Laserchron Center are thanked for their help during U-Pb zircon dating. We are grateful for comments from Paul Fitzgerald and Suzanne Baldwin that improved this manuscript.

Conflicts of Interest

The authors declare no conflict of interest.

References

1. Xiao, W.; Windley, B.; Hao, J.; Zhai, M. Accretion leading to collision and the Permian Solonker suture, Inner Mongolia, China: Termination of the central Asian orogenic belt. *Tectonics* **2003**, *22*, 1069:1–1069:20.

2. Windley, B.; Alexeiev, D.; Xiao, W.; Kröner, A.; Badarch, G. Tectonic models for accretion of the Central Asian Orogenic Belt. *J. Geol. Soc.* **2007**, *164*, 31–47.
3. Şengör, A.; Natal'in, B.; Burtman, V. Evolution of the Altaid tectonic collage and Paleozoic crustal growth in Eurasia. *Nature* **1993**, *264*, 299–307.
4. Şengör, A.; Natal'in, B. Paleotectonics of Asia: Fragments of a Synthesis. In *The Tectonic Evolution of Asia*; Cambridge University Press: Cambridge, UK, 1996; pp. 486–640.
5. Helo, C.; Hegner, E.; Kröner, A.; Badarch, G.; Tomurtogoo, O.; Windley, B.; Dulski, P. Geochemical signature of Paleozoic accretionary complexes of the Central Asian Orogenic Belt in South Mongolia: Constraints on arc environments and crustal growth. *Chem. Geol.* **2006**, *227*, 236–257.
6. Badarch, G.; Cunningham, W.; Windley, B. A new terrane subdivision for Mongolia: Implications for the Phanerozoic crustal growth of Central Asia. *J. Asian Earth Sci.* **2002**, *21*, 87–110.
7. Demoux, A.; Kröner, A.; Liu, D.; Badarch, G. Precambrian crystalline basement in southern Mongolia as revealed by SHRIMP zircon dating. *Int. J. Earth Sci.* **2009**, *98*, 1365–1380.
8. Salnikova, E.; Kozakov, I.; Kotov, A.; Kröner, A.; Todt, W.; Bibikova, E.; Nutman, A.; Yakovleva, S.; Kovach, V. Age of Palaeozoic granites and metamorphism in the Tuvino-Mongolian Massif of the Central Asian Mobile Belt: Loss of a Precambrian microcontinent. *Precambrian Res.* **2001**, *110*, 143–154.
9. Wang, T.; Zheng, Y.; Gehrels, G.; Mu, Z. Geochronological evidence for existence of South Mongolian microcontinent—A zircon U-Pb age of granitoid gneisses from the Yagan-Onch Hayrhan metamorphic core complex. *Chin. Sci. Bull.* **2001**, *46*, 2005–2008.
10. Yarmolyuk, V.; Kovalenko, V.; Sal'nikova, E.; Kozakov, I.; Kotov, A.; Kovach, V.; Vladykin, N.; Yakovleva, S. U-Pb age of syn- and post-metamorphic granitoids of South Mongolia: Evidence for the presence of Grenvillides in the Central Asia Fold belt. *Dokl. Earth Sci.* **2005**, *404*, 986–990.
11. Peltzer, G.; Tapponnier, P. Formation and evolution of strike-slip faults, rifts, and basins during the India–Asia collision: An experimental approach. *J. Geophys. Res.* **1988**, *93*, 15085–15117.
12. Houseman, G.; England, P. *Crustal Thickening versus Lateral Expulsion in the Indian–Asian Continental Collision*; Yin, A., Harrison, M., Eds.; Cambridge University Press: Cambridge, UK, 1996; pp. 3–17.
13. Yin, A.; Harrison, M. Geologic evolution of the Himalayan-Tibetan Orogen. *Annu. Rev. Earth Planet. Sci.* **2000**, *28*, 211–279.
14. Cunningham, W. Active intracontinental transpressional mountain building in the Mongolian Altai: Defining a new class of orogen. *Earth Planet. Sci. Lett.* **2005**, *240*, 436–444.
15. De Grave, J.; Buslov, M.; van den Haute, P. Distant effects of India–Eurasia convergence and Mesozoic intracontinental deformation in Central Asia: Constraints from apatite fission-track thermochronology. *J. Asian Earth Sci.* **2007**, *29*, 188–204.
16. Cunningham, W.D. Tectonic Setting and Structural Evolution of the Late Cenozoic Gobi Altai Orogen. In *The Evolving Continents: Understanding Processes of Continental Growth*; Special Publication 338; Kusky, T.M., Zhai, M.G., Xiao, W., Eds.; The Geological Society of London: London, UK, 2010; pp. 361–387.

17. Demoux, A.; Kröner, A.; Badarch, G.; Jian, P.; Tomurhuu, D.; Wingate, T. Zircon ages from the Baydrag Block and the Bayankhongor ophiolite zone: Time constraints on Late Neoproterozoic to Cambrian subduction- and accretion-related magmatism in Central Mongolia. *J. Geol.* **2009**, *117*, 377–397.
18. Yanshin, A. *Map of Geological Formations of the Mongolian People's Republic*; Academia Nauka: Moscow, USSR, 1989; Scale 1:1,500,000.
19. Tomurtogoo, O. *General Map of Mongolia*; General Directorate of Mineral Research and Exploration: Ankara, Turkey, 1999; Scale 1:1,000,000.
20. Dorjnamjaa, D.; Badarch, G.; Orolmaa, D. The Geodynamic Evolution of the Mobile Fold Belts of the Territory of Mongolia. In *Reconstruction of the Paleo-Asian Ocean*, Proceedings of the 29th International Geological Congress, Kyoto, Japan, 24 August–3 September 2012; Part B, pp. 71–84.
21. Kovalenko, V.; Yarmolyuk, V.; Kovach, V.; Kotov, A.; Kozakov, I.; Salnikoval, E.; Larin, A. Isotope provinces, mechanisms of generation and sources of the continental crust in the Central Asian mobile belt: Geological and isotopic evidence. *J. Asian Earth Sci.* **2004**, *23*, 605–627.
22. Yarmolyuk, V.; Kovach, V.; Kovalenko, V.; Terent'eva, L.; Kozakov, I.; Kotov, A.; Eenjin, G. Isotopic composition of the Hercynian crust of southern Mongolia: Substantiation of the Hercynian Juvenile crust-forming event. *Dokl. Earth Sci.* **2007**, *417*, 1178–1182.
23. Yarmolyuk, V.; Kovalenko, V.; Sal'nikova, E.; Kovach, V.; Kozlovsky, A.; Kotov, A.; Lebedev, V. Geochronology of igneous rocks and formation of the Late Paleozoic South Mongolian active margin of the Siberian Continent. *Stratigr. Geol. Correl.* **2008**, *16*, 162–181.
24. Lamb, M.; Hanson, A.; Graham, S.; Badarch, G.; Webb, L. Left-lateral sense of offset of Upper Proterozoic to Paleozoic features across the Gobi Onon, Tost, and Suunbayan faults in southern Mongolia and implications for other central Asian faults. *Earth Planet. Sci. Lett.* **1999**, *173*, 183–194.
25. Webb, L.; Graham, S.; Johnson, C.; Badarch, M. Occurrence, age, and implications of the Yagan-Onch Hayrhan metamorphic core complex, southern Mongolia. *Geology* **1999**, *27*, 143–146.
26. Webb, L.E.; Johnson, C.L.; Minjin, C. Late Triassic sinistral shear in the East Gobi Fault Zone, Mongolia. *Tectonophysics* **2010**, *495*, 246–255.
27. Zheng, Y.; Zhang, Q.; Wang, Y.; Lui, R.; Wang, S.; Zuo, G.; Wang, S.; Lkaasuren, B.; Badarch, G.; Badamgarav, Z. Great Jurassic thrust sheets in Beishan (North Mountains)—Gobi areas of China and southern Mongolia. *J. Struct. Geol.* **1996**, *18*, 1111–1126.
28. Webb, L.; Johnson, C. Tertiary strike-slip faulting in southeastern Mongolia and implications for Asian tectonics. *Earth Planet. Sci. Lett.* **2006**, *241*, 323–363.
29. Johnson, C.L.; Webb, L.; Graham, S.; Hendrix, M.; Badarch, G. Sedimentary and structural records of late Mesozoic high-strain extension and strain partitioning, East Gobi basin, southern Mongolia. *GSA Mem.* **2001**, *194*, 413–433.
30. Heumann, M.; Johnson, C.; Webb, L.; Taylor, J. Mesozoic-Cenozoic reconstruction of the East Gobi Fault Zone, Southeastern Mongolia. In Proceedings of 2009 American Geophysical Union Fall Meeting, San Francisco, CA, USA, 14–18 December 2009; abstract #T41E-05.

31. Heumann, M. Paleozoic-Cenozoic Evolution of the East Gobi Fault Zone, Southern Mongolia: A Protracted Record of Intracontinental Deformation and Basin Evolution, with Implications for Tectonics in Eurasia. Ph.D. Thesis, University of Utah, Salt Lake City, UT, USA, 8 October 2010.
32. Johnson, C. Polyphase evolution of the East Gobi basin: Sedimentary and structural records of Mesozoic-Cenozoic intraplate deformation in Mongolia. *Basin Res.* **2004**, *16*, 79–99.
33. Prost, G. Tectonics and hydrocarbon systems of the East Gobi basin, Mongolia. *AAPG Bull.* **2004**, *88*, 483–513.
34. Johnson, C.; Ritts, B. Plate Interior Polyphase Basins. In *Recent Advances in Tectonics of Sedimentary Basins*; Blackwell Science: West Sussex, UK, 2012; pp. 567–582.
35. Zheng, Y.; Wang, S.; Wang, Y. An enormous thrust nappe and extensional metamorphic core complex discovered in Sino-Mongolian boundary area. *Sci. China* **1991**, *34*, 1145–1154.
36. Zheng, Y.; Zhang, Q. The Yagan metamorphic core complex and extensional detachment fault in Inner Mongolia, China. *Acta Geol. Sin.* **1994**, *7*, 125–137.
37. Johnson, C.; Amory, J.; Zinniker, D.; Lamb, M.; Graham, S.; Affolter, M.; Badarch, G. Sedimentary response to arc-continent collision, Permian, southern Mongolia. *GSA Spec. Pap.* **2008**, *436*, 363–390.
38. Lamb, M.; Badarch, G. Paleozoic sedimentary basins and volcanic arc systems of southern Mongolia: New geochemical and petrographic constraints. *GSA Mem.* **2001**, *194*, 117–150.
39. Blight, J.; Crowley, Q.; Petterson, M.; Cunningham, D. Granites of the Southern Mongolia Carboniferous Arc: New geochronological and geochemical constraints. *Lithos* **2010**, *116*, 35–52.
40. Lamb, M.; Cox, D. New $^{40}\text{Ar}/^{39}\text{Ar}$ age data and implications for porphyry copper deposits of Mongolia. *Econ. Geol.* **1998**, *93*, 524–529.
41. Watanabe, Y.; Stein, H. Re-Os ages for the Erdenet and Tsagaan Suvarga porphyry Cu-Mo deposits, Mongolia, and tectonic implications. *Econ. Geol.* **2000**, *95*, 1537–1542.
42. Perelló, P.; Cox, D.; Garamjav, D.; Diakov, S.; Schissel, D.; Munkhbat, T.; Oyun, G. Oyu Tolgoi, Mongolia: Siluro-Devonian porphyry Cu-Au-(Mo) and high-sulfidation Cu mineralization with a Cretaceous chalcocite blanket. *Econ. Geol.* **2001**, *96*, 1407–1428.
43. Heumann, M.; Johnson, C.; Webb, L.; Taylor, J.; Jalball, U.; Minjin, C. Paleogeographic reconstruction of a late Paleozoic arc collision zone, southern Mongolia. *GSA Bull.* **2012**, *124*, 1514–1534.
44. Graham, S.; Hendrix, M.; Johnson, C.B.D.; Badarch, G.; Amory, J.; Porter, J.; Barsbold, R.; Webb, L.; Hacker, B. Sedimentary record and tectonic implications of Mesozoic rifting in southeast Mongolia. *GSA Bull.* **2001**, *113*, 1560–1579.
45. Meng, Q.; Hu, J.; Jin, J.; Zhang, Y.; Xu, D. Tectonics of the late Mesozoic wide extensional basin system in the China-Mongolia border region. *Basin Res.* **2003**, *15*, 297–415.
46. Passchier, C.; Trouw, R. *Microtectonics*, 2nd ed.; Springer-Verlag: Berlin, Germany, 2005.
47. Gehrels, G.; Valencia, V.; Pullen, A. Detrital zircon geochronology by Laser Ablation Multicollector ICPMS at the Arizona LaserChron Center. *Paleontol. Soc. Pap.* **2006**, *12*, 67–76.
48. Gehrels, G.; Valencia, V.; Ruiz, J. Enhanced precision, accuracy, efficiency, and spatial resolution of U-Pb ages by laser ablation–multicollector–inductively coupled plasma–mass spectrometry. *Geochem. Geophys. Geosyst.* **2008**, *9*, Q03017:1–Q03017:13.

49. Johnston, S.; Gehrels, S.; Valencia, V.; Ruiz, J. Small-volume U–Pb zircon geochronology by laser ablation-multicollector-ICP-MS. *Chem. Geol.* **2009**, *259*, 218–229.
50. Stacey, J.; Kramers, J. Approximation of terrestrial lead isotope evolution by a twostage model. *Earth Planet. Sci. Lett.* **1975**, *26*, 207–221.
51. The Age Pick Macro Add-On for Microsoft Excel. Available online: https://docs.google.com/file/d/0B9ezu34P5h8eNWRkMGZkNTgtZDdhOC00OGZkLTkxNjUtYzY5M2UzYjU1ZmVi/edit?hl=en_US&pli=1 (accessed on 12 August 2013).
52. Ludwig, K. *Isoplot 3.60*; Berkeley Geochronology Center: Berkeley, CA, USA, 2008. Available online: http://www.bgc.org/isoplot_etc/isoplot.html (accessed on 12 August 2013).
53. Whitney, D.; Evans, B. Abbreviations for names of rock-forming minerals. *Am. Mineral.* **2010**, *95*, 185–187.
54. Hoskin, P.; Schaltegger, U. The composition of zircon and igneous and metamorphic petrogenesis. *Rev. Mineral. Geochem.* **2003**, *53*, 27–62.
55. Vernon, R. *A Practical Guide to Rock Microstructure*; Cambridge University Press: Cambridge, UK, 2004.
56. Geisler, T.; Pidgeon, R.; van Broswijk, W.; Kurtz, R. Transport of uranium, thorium, and lead in metamict zircon under low-temperature hydrothermal conditions. *Chem. Geol.* **2002**, *191*, 141–154.
57. Ruzhentsev, S.; Pospelov, I.; Badarch, G. Tectonics of the Mongolian Indosinides. *Geotectonics* **1989**, *23*, 476–487.
58. Ruzhentsev, S.; Pospelov, I. The South Mongolian Variscan fold system. *Geotectonics* **1992**, *26*, 383–395.
59. Zorin, Y.; Belichenko, V.; Turitanov, E.; Kozhenvnikov, V.; Ruzhentsev, S.; Dergunov, A.; Filippova, I.; Tomurtoogoo, O.; Arvisbaatar, N.; *et al.* The South-Siberia-Central Mongolia transect. *Tectonophysics* **1993**, *225*, 361–378.
60. Lamb, M.; Badarch, G. Paleozoic sedimentary basins and volcanic-arc systems of southern Mongolia; new stratigraphic and sedimentologic constraints. *Int. Geol. Rev.* **1997**, *39*, 542–576.
61. Kovalenko, V.; Yarmolyuk, V.; Sal'nikova, E.; Kozlovsky, A.; Kotov, A.; Kovack, V.; Savatenkov, V.; Vladykin, N.; Ponomarchuk, V. Geology, geochronology, and geodynamics of the Khan Bogd alkali granite pluton of Southern Mongolia. *Geotectonics* **2006**, *40*, 450–466.
62. Chen, B.; Jahn, B.; Wilde, S.; Xu, B. Two contrasting Paleozoic magmatic belts in northern Inner Mongolia, China: Petrogenesis and tectonic implications. *Tectonophysics* **2000**, *328*, 157–182.
63. Chen, B.; Jahn, B.; Tian, W. Evolution of the Solonker suture zone: Constraints from zircon U-Pb ages, Hf isotopic ratios and whole-rock Nd-Sr isotope compositions of subduction- and collision-related magmas and forearc sediments. *J. Asian Earth Sci.* **2009**, *34*, 245–257.
64. Wu, F.; Sun, D.; Li, H.; Jahn, B.; Wilde, S. A-type granites in northeastern China: Age and geochemical constraints on their petrogenesis. *Chem. Geol.* **2002**, *187*, 143–173.
65. Wang, T.; Zheng, Y.; Li, T.; Gao, Y. Mesozoic granitic magmatism in extensional tectonics near the Mongolian border with China and its implications for crustal growth. *J. Asian Earth Sci.* **2004**, *23*, 715–729.

66. Zhang, S.; Zhao, Y.; Song, B.; Hu, J.; Liu, S.; Yang, Y.; Chen, F.; Liu, X.; Liu, J. Contrasting Late Carboniferous and Late Permian-Middle Triassic intrusive suites from the northern margin of the North China craton: Geochronology, petrogenesis, and tectonic implications. *Geol. Soc. Am. Bull.* **2009**, *121*, 191–200.
67. Davis, G.; Xu, B.; Zheng, Y.; Zhang, W. Indosinian extension in the Solonker suture zone: The Sonid Zuopi metamorphic core complex, Inner Mongolia, China. *Earth Sci. Front.* **2004**, *11*, 135–144.
68. Yin, A. Cenozoic tectonic evolution of Asia: A preliminary synthesis. *Tectonophysics* **2010**, *488*, 293–325.
69. Zhao, G.; Wilde, S.; Cawood, P.; Sun, M. Archean blocks and their boundaries in the North China Craton: Lithological, geochemical, structural and P-T path constraints and tectonic evolution. *Precambrian Res.* **2001**, *107*, 45–73.
70. Zhai, M.; Shao, J.; Hao, J.; Peng, P. Geological signature and possible position of the North China Block in the supercontinent Rodinia. *Gondwana Res.* **2003**, *6*, 171–183.
71. Cope, T.; Ritts, B.; Darby, B.; Fildani, A.; Graham, S. Late Paleozoic sedimentation on the northern margin of the North China Block; Implications for regional tectonics and climate change. *Int. Geol. Rev.* **2005**, *47*, 270–296.
72. Darby, B.; Gehrels, G. Detrital zircon reference for the North China Block. *J. Asian Earth Sci.* **2006**, *26*, 637–648.
73. Jian, P.; Liu, D.; Kroner, A.; Windley, B.; Shi, Y.; Zhang, F.; Shi, G.; Miao, L.; Zhang, W.; Zhang, Q.; *et al.* Time scale of an early to mid-Paleozoic orogenic cycle of the long-lived Central Asian Orogenic Belt, Inner Mongolia of China: Implications for continental growth. *Lithos* **2008**, *101*, 233–259.
74. Zhang, J.; Mattinson, C.; Meng, F.; Wan, Y.; Tung, K. Polyphase tectonothermal history recorded in granulitized gneisses from the north Qaidam HP/UHP metamorphic terrane, western China: Evidence from zircon U-Pb geochronology. *GSA Bull.* **2010**, *120*, 732–749.
75. Zhao, G.; Wilde, S.; Sun, M.; Guo, J.; Kroner, A.; Li, S.; Li, X.; Zhang, J. SHRIMP U-Pb geochronology of the Hui'an complex: Constraints on Late Archean to Paleoproterozoic magmatic and metamorphic events in the Trans-North China Orogen. *Am. J. Sci.* **2008**, *308*, 270–303.
76. Li, Q.; Chen, F.; Guo, J.; Li, X.; Yang, Y.; Siebel, W. Zircon ages and Nd-Hf isotopic composition of the Zhaertai Group (Inner Mongolia): Evidence for early Proterozoic evolution of the northern North China Craton. *J. Asian Earth Sci.* **2007**, *30*, 573–590.
77. Lu, S.; Li, H.; Zhang, C.; Niu, G. Geological and geochronological evidence for the Precambrian evolution of the Tarim Craton and surrounding continental fragments. *Precambrian Res.* **2008**, *160*, 94–107.
78. Gehrels, G.; Wang, X. Magmatic history of the northeastern Tibetan Plateau. *J. Geophys. Res.* **2003**, *108*, 2423:1–2423:14.
79. Rojas-Agramonte, Y.; Kroner, A.; Demoux, A.; Xia, X.; Wang, W.; Donskaya, T.; Liu, D.; Sun, M. Detrital and xenocrystic zircon ages from Neoproterozoic and Palaeozoic arc terranes of Mongolia: Significance for the origin of crustal fragments in the Central Asian Orogenic Belt. *Gondwana Res.* **2011**, *19*, 751–763.

80. Hendrix, M.; Graham, S.; Carroll, A.; Sobel, E.; McKnight, C.; Schulein, B.; Wang, Z. Sedimentary record and climatic implications of recurrent deformation in the Tian Shan: Evidence from Mesozoic strata of the north Tarim, south Junggar, and Turpan basins, northwest China. *GSA Bull.* **1992**, *104*, 53–79.
81. Hendrix, M.; Beck, M.; Badarch, G.; Graham, S. Triassic synorogenic sedimentation in southern Mongolia: Early effects of intracontinental deformation. *GSA Mem.* **2001**, *194*, 389–412.
82. Traynor, J.; Sladen, C. Tectonic and stratigraphic evolution of the Mongolian People's Republic and its influence on hydrocarbon geology and potential. *Mar. Petrol. Geol.* **1995**, *12*, 35–52.
83. Taylor, J.; Webb, L.; Johnson, C.; Heumann, M. Constraints on Mesozoic and Tertiary Brittle Faulting in the Southern East Gobi Fault Zone, Southeastern Mongolia. In Proceedings of 2007 American Geophysical Union Fall Meeting, San Francisco, CA, USA, 10–14 December 2007; Abstract #V23C-1558.
84. Taylor, J.P. Tectonic History of the East Gobi Fault Zone, Southeastern Mongolia: An Integrated Study Using Structural Geology, Geochronology, and Thermochronology. Ph.D. Thesis, Syracuse University, Syracuse, NY, USA, 13 December 2010.
85. Taylor, J.; Webb, L.; Johnson, C.; Heumann, M. Strike-Slip and Exhumation History of the East Gobi Fault Zone, Southeastern Mongolia, with Emphasis of the Cenozoic Era. In Proceedings of 2009 Portland GSA Annual Meeting, Portland, OR, USA, 18–21 October 2009; Paper No. 254-3.

© 2013 by the authors; licensee MDPI, Basel, Switzerland. This article is an open access article distributed under the terms and conditions of the Creative Commons Attribution license (<http://creativecommons.org/licenses/by/3.0/>).